

1 Decade-long Ozone Profile Record from Suomi NPP OMPS Limb
2 Profiler: Assessment of Version 2.6 Data

3 N.A. Kramarova¹, P. Xu², J.B. Mok³, P.K. Bhartia^{1,*}, G. Jaross¹, L. Moy³, Z. Chen³, S.
4 Frith³, M. DeLand³, D. Kahn³, G. Labow³, J. Li³, E. Nyaku³, C. Weaver⁴, J. Ziemke⁵, S. Davis⁶,
5 and Y. Jia^{6,7}

6
7 ¹NASA GSFC, Greenbelt, MD.

8 ²SAIC, Greenbelt, MD;

9 ³SSAI, Greenbelt, MD;

10 ⁴ESSIC, College Park, MD;

11 ⁵Morgan State University, Baltimore, MD;

12 ⁶NOAA Chemical Sciences Laboratory, Boulder, CO;

13 ⁷Cooperative Institute for Research in Environmental Sciences, University of Colorado at
14 Boulder, Boulder, CO;

15 *Emeritus

16
17 Corresponding author: Natalya Kramarova (natalya.a.kramarova@nasa.gov)

18
19 **Key Points:**

- 20 • OMPS Limb Profiler
21 • Stratospheric Ozone Profiles
22 • Ozone Recovery
23

Abstract

We evaluate a decadal ozone profile record derived from the Suomi National Polar-orbiting Partnership (SNPP) Ozone Mapping and Profiler Suite (OMPS) Limb Profiler (LP) satellite instrument. In 2023, the OMPS LP data were re-processed with the new version 2.6 retrieval algorithm that combines measurements from the ultraviolet (UV) and visible (VIS) parts of the spectra and employs the second order Tikhonov regularization to retrieve a single vertical ozone profile between 12.5 km (or cloud tops) and 57.5 km with the vertical resolution of about 1.9 - 2.5 km between 20-55 km. The algorithm uses radiances measured at six UV ozone-sensitive wavelengths (295, 302, 306, 312, 317 and 322 nm) paired with 353 nm, and one VIS wavelength at 606 nm combined with 510 nm and 675 nm to form a triplet. Each wavelength pair or triplet is used over a limited range of tangent altitudes where the sensitivity to ozone changes are strongest. A new implemented aerosol correction scheme is based on a gamma-function particle size distribution. Numerous calibration changes that affected ozone retrievals were also applied to measured LP radiances, including updates in altitude registration, radiometric calibration, stray light, and spectral registration. The key version 2.6 improvement is the reduction in relative drifts between LP ozone and correlative measurements, linked previously to a drift in the version 2.5 LP altitude registration. We compare LP ozone profiles with those from Aura Microwave Limb Sensor (MLS) to quantify ozone changes in version 2.6.

Plain Language Summary

The Montreal Protocol protects the Earth's ozone layer by regulating the production and usage of ozone-depleting substances. As a result of this international treaty, we expect stratospheric ozone to increase over time. A series of OMPS Limb Profilers (LP) was designed to ensure continuous spaceborne capabilities for detecting changes in the stratospheric ozone distribution over several decades. The ozone record from the first OMPS LP on board of the Suomi NPP mission spans more than 11 years, from April 2012 to the present. A statistically significant positive drift in the previous version 2.5 of LP ozone data, linked to a drift in the LP altitude registration, has compromised its fitness to accurately detect ozone trends. In this paper, we introduce the new version 2.6 OMPS LP ozone dataset with improved stability. We found a substantial reduction in relative drifts between LP ozone and correlative measurements. Therefore, the version 2.6 LP ozone can be used with higher confidence for monitoring and quantifying stratospheric ozone recovery.

55 **1 Introduction**

56 NASA has pioneered space-borne observations of the ozone layer by developing the
57 Backscattered Ultraviolet (BUV) technique in the 1960s to measure total column ozone and ozone
58 profile. The first BUV instrument, on NASA's Nimbus-4 platform, was launched more than 50
59 years ago in 1970. Ozone profile observations were continued with the improved Solar
60 Backscattered Ultraviolet (SBUV) sensor on board of Nimbus-7, and then by the series of the
61 SBUV/2 instruments flown on seven NOAA polar orbiting missions between 1984 and the 2010s.

62 The discovery of the Antarctic ozone hole in 1985 (e.g. Farman et al., 1985; Stolarski et
63 al., 1986) triggered public concerns world-wide. Since that time the development of ozone
64 measurement techniques have been guided by international agreements and public policies aimed
65 to preserve the Earth's ozone layer. The US Clean Air Act specifically mandates NASA and
66 NOAA to monitor the ozone layer, and the international community depends upon these
67 measurements for periodic assessments of the integrity of the ozone layer required under the
68 Montreal Protocol (WMO, 2022).

69 Given the limited profiling capability of the SBUV/2 sensor, NOAA developed a suite of
70 OMPS sensors for the NOAA/NASA joint National Polar-orbiting Operational Environmental
71 Satellite System (NPOESS). In addition to a nadir mapping sensor (OMPS-NM) based on NASA's
72 Total Ozone Mapping Spectrometer (TOMS) instrument, and a nadir profiler sensor (OMPS-NP)
73 based on the Solar Backscattered UV (SBUV/2) instrument, OMPS also has a limb scattering
74 sensor (OMPS-LP). OMPS-LP is based on technologies developed by NASA in the 1980s and
75 1990s for the Shuttle Ozone Limb Sounding Experiment flown on STS-87 and STS-107 (Flittner
76 et al., 2000; McPeters et al., 2000). Though OMPS does not measure a large suite of trace gases
77 that influence ozone photochemistry, it fully satisfies the public policy need to monitor the ozone
78 layer (NASA, 2023). Space-borne observations with operational OMPS suites will be extended
79 into the next two decades.

80 Owing to the regulations imposed by the Montreal Protocol, the levels of anthropogenically
81 produced chlorine and bromine compounds that destroy the ozone layer have been gradually
82 declining since the early 2000s. Scientists found unambiguous increases of ~1.0–2.2% per decade
83 in upper-stratospheric ozone over 2000–2020 period (WMO, 2022), driven by declines in ozone-
84 depleting substances and increases in greenhouse gases (GHGs). Observations of the vertical
85 ozone distribution derived from OMPS are used to evaluate the health of the ozone layer.

86 In this study we present and evaluate the OMPS LP version 2.6 ozone data product. Section
87 2 describes version 2.6 processing and documents changes in Level 1 (calibrated radiances) and
88 Level 2 (ozone profile retrievals) algorithms. Section 3 evaluates SNPP OMPS LP profiles over a
89 decade by comparing with Aura MLS. A summary is provided in Section 4. This study will be
90 complemented by an upcoming comprehensive validation paper where OMPS LP will be
91 compared with an extended set of correlative satellite and ground-based observations.

92 **2 Ozone Mapping and Profiler Suite**

93 **2.1 OMPS Limb Profiler**

94 The Ozone Mapping and Profiler Suite (OMPS) was designed to provide profile and total
95 ozone measurements (Flynn et al., 2006), extending the long-term satellite ozone records from
96 NASA/NOAA missions like TOMS, Ozone Mapping Instrument (OMI), SBUV/2, Stratospheric
97 Aerosol and Gas Experiment (SAGE) and MLS. SNPP OMPS, launched in October 2011,
98 comprises three complementary ozone sensors – Limb Profiler (LP), Nadir Profiler (NP) and Nadir
99 Mapper (NM) - that scan the same region of the atmosphere from Earth's surface to the mesosphere
100 within minutes to measure the global ozone distribution at high spatial and vertical resolution
101 (Kramarova et al., 2014). NOAA-20 (formerly JPSS-1) OMPS, launched in October 2017,
102 includes only the two nadir sensors, but NOAA-21 (JPSS-2), launched in November 2022, has the
103 Limb Profiler as well. Two more OMPS will be launched in the next decade including all 3 sensors
104 on board of JPSS-3 and JPSS-4 missions. In this paper we focus on the ozone profile record derived
105 from the SNPP OMPS LP. The operational observations with SNPP OMPS LP started in April
106 2012, and the record now exceeds 12 years.

107 The OMPS LP sensor measures solar irradiances scattered from the atmospheric limb in
108 the ultraviolet (UV) and visible (VIS) spectral ranges (between 290 and 1000 nm) with variable
109 spectral resolution that increases from about 1 nm at 290 nm to 30 nm at longer wavelengths near
110 1000 nm. The instrument is mounted at the back of the spacecraft and collects measurements by
111 viewing the atmospheric limb along the satellite track. The LP has a 1.85° vertical field of view
112 (FOV) and covers 100 km, but because of spacecraft pointing variations it reliably measures
113 scattered light between the ground and ~80 km throughout the orbit. Scattered light is projected to
114 a 2-dimensional Charge Coupled Device (CCD) detector. The vertical sampling of LP
115 measurements, determined by the CCD pixel sampling, is ~1 km, but the actual instantaneous FOV
116 of each pixel is about 1.2 km. To avoid saturation of the CCD pixels and to capture measurements

117 over the entire spectral and vertical range, the OMPS LP splits each vertical profile into two
118 images: low altitude (bright) signals are measured with the small aperture, whereas the high
119 altitude (low intensity) signals are measured with the large aperture. The full spectra from both
120 apertures are produced every 19 seconds. Due to bandwidth limitations, data from all CCD pixels
121 can not be downloaded from the instrument to the ground during the normal operations, and only
122 a relatively small subset of pixels (so called the Sample Table) becomes available for the retrieval
123 process. The downloaded pixels from the two spectra are then stitched together and mapped onto
124 the regular spectral and vertical grids (Level 1G). The instrument has three slits separated
125 horizontally by 4.25° (about 250 km) to increase the cross-track coverage, but in this study, we
126 focus only on measurements obtained from the center slit aligned with the satellite ground track.

127 2.2 Version 2.6 Processing

128 The first version of ozone profiles derived from the SNPP OMPS LP was released soon
129 after the beginning of operational observations in April 2012 (Rault and Loughman, 2013). In July
130 2014 version 2 of the LP ozone profile dataset was released which included corrections for the
131 sensor pointing and simplification in the retrieval algorithm (Xu et al., 2014). Version 2.5 was
132 released in July 2017 (Kramarova et al., 2018). Both version 2 and version 2.5 datasets have been
133 produced using a modified version of the OMPS LP retrieval algorithm (Rault and Loughman,
134 2013), and detailed description of version 2 and version 2.5 datasets and validation results are
135 summarized by Kramarova et al. (2018). Here we present a new version 2.6 of the LP ozone
136 profiles, released in March 2023. In this section we describe the key changes implemented in the
137 Level 1 (Sec. 2.2.1) and Level 2 (Sec. 2.2.2) algorithms for the processing of version 2.6 data.

138 LP ozone retrievals are reported in daily files that contain ozone number density retrievals
139 from the center slit only (see Sec. 4.1) along with geolocation information and quality flags
140 (Kramarova and DeLand, 2023). For users' convenience, for each ozone measurement we also
141 report atmospheric pressure and temperature profiles that are derived from the Goddard Earth
142 Observing System (GEOS) Forward Processing for Instrument Teams (FP-IT) product produced
143 by the NASA Global Modeling Assimilation Office (GMAO) (Gelaro et al., 2017; Lucchesi,
144 2013).

145 2.2.1 SNPP OMPS LP calibration

146 In this section we describe instrumental calibrations applied to LP radiances in Level 1
147 processing. Radiometric errors and errors in sensor pointing (primarily those related to altitude

148 registration errors) are the two main sources of errors in the limb scattering technique affecting
149 the accuracy of retrieved ozone profiles.

150 Two-dimensional (spectral-spatial) CCD detectors are susceptible to internally scattered
151 stray light where photons from bright parts of a scene can scatter to the CCD regions with a weaker
152 signal. Jaross et al. (2014) describe the stray light (SL) corrections implemented in the version 2
153 production that were based on the pre-launch point-spread-function (PSF) measurements. In
154 version 2.5, empirical adjustments were applied to the two-dimensional PSFs used in the VIS
155 range. These PSFs predict the SL content in all detector pixels as a fraction of the measured source
156 signal at a given wavelength and altitude. The total SL in a pixel is the sum of the contributing
157 fractions from all source wavelengths and altitudes. The empirical technique, previously applied
158 to Global Ozone Monitoring by Occultation of Stars (GOMOS) (Taha et al., 2008) and SAGE III
159 (Rault, 2005), uniformly scales all the PSF fractions at a given source wavelength so that the total
160 predicted SL at 80 km and above matches the measured signal at these altitudes and wavelengths.

161 In version 2.6, the SL correction has been updated. The version 2.5 empirical corrections
162 were removed. Instead, the tails of the PSFs for both UV and VIS/NIR have been increased by
163 about 12% to account for the apparent underestimation of high altitude stray light photons. A
164 correction has been added to account for in-band scattering by the primary telescope mirror. Such
165 scattering is likely a result of particulate contamination on the mirror surface. This correction was
166 characterized during pre-launch testing but has been scaled by factors of 1.5 and 3 for the LP center
167 and right (west) slits, respectively, at VIS/NIR wavelengths. The correction was not altered for the
168 left slit or UV measurements from all 3 slits. Finally, a correction for out-of-band stray light
169 originating longward of 1000 nm was also introduced. Comparisons between measured and
170 modeled radiances suggest that the changes were most effective at VIS wavelengths at tangent
171 heights above 40 km. Residual stray light at UV wavelengths was already low in version 2.5 data.

172 The LP static radiometric calibration has been revised in the version 2.6 processing to use
173 two-dimensionally (spectral x spatial) smoothed pre-launch albedo coefficients
174 (radiance/irradiance). The “Day 1” calibrations are now based on solar measurements from orbit
175 number 1864 on March 7th, 2012. The “Day 1” wavelength scale assignment has also been updated
176 based on measurements from this orbit. The solar irradiance measurements taken on “Day 1” are
177 used to calculate sun-normalized radiances. This normalization is not updated over the mission
178 lifetime though solar measurements occur every week. Instead, starting in version 2.6, solar

179 measurements following “Day 1” are used to update Earth radiance calibrations. Corrections,
180 derived by applying 5-pixel spectral smoothing of the solar data, do not exceed 3% for the mission
181 at any wavelength (290 – 1000 nm), nor at any spatial location. There is no indication these
182 radiometric adjustments had a significant effect on the profile ozone time dependence because the
183 altered calibration is mostly independent of altitude.

184 Version 2.6 utilizes these same weekly solar measurements to derive seasonal and long-
185 term changes in wavelength registration. A seasonal spectral shift of amplitude 0.25 pixels was
186 previously assigned to the data in a static pattern every year. A 1-pixel shift corresponds to
187 approximately 0.75 nm band center shifts at 300 nm and 17 nm shifts at 1000 nm due to the non-
188 linear dispersion of the LP instrument. Dynamic use of the solar measurements now allows year-
189 to-year variations in the seasonal pattern, and can account for long-term drifts in pixel band center
190 wavelengths. The mean change in wavelength registration over the first 10 years of the S-NPP
191 mission is approximately 0.1 pixels. Changes in pixel band center wavelengths through each orbit,
192 a result of thermally induced changes in spectrometer optics pointing, are registered the same as
193 in previous versions (Jaross et al., 2014). As with the radiometric calibrations described in the
194 preceding paragraph, spectral shifts are largely independent of altitude and thus have little effect
195 on the altitude-normalized measurements used for ozone retrievals.

196 Accurate and stable altitude registration of limb scattering measurements is very important
197 for retrieving high-quality ozone profiles suitable for climate studies, since an error of just 100 m
198 in altitude can result in as much as a 3% error in ozone at altitudes above 35 km. The primary
199 source of knowledge for the sensor pointing comes from the SNPP spacecraft attitude
200 determination system consisting of two star-tracking devices. Despite that, a significant offset (~
201 1.4 km, adjusted in version 2) in the LP pointing was discovered shortly after launch, some of it
202 apparently the result of a misalignment of the attitude control frame and the spacecraft body
203 frame. The SNPP VIIRS instrument team also observed a shift. To complicate this matter,
204 thermally-induced distortions in the LP optics resulted in as much as a 1 km (depending on the
205 slit) change in pointing from the ground to orbit. These same distortions result in measurable
206 changes in wavelength and pointing during every orbit. Our baseline approach to LP altitude
207 registration is to assume that the spacecraft attitude information is accurate but that additional
208 adjustments are needed to account for distortions originating within OMPS. This assumption has
209 one notable exception that we describe below.

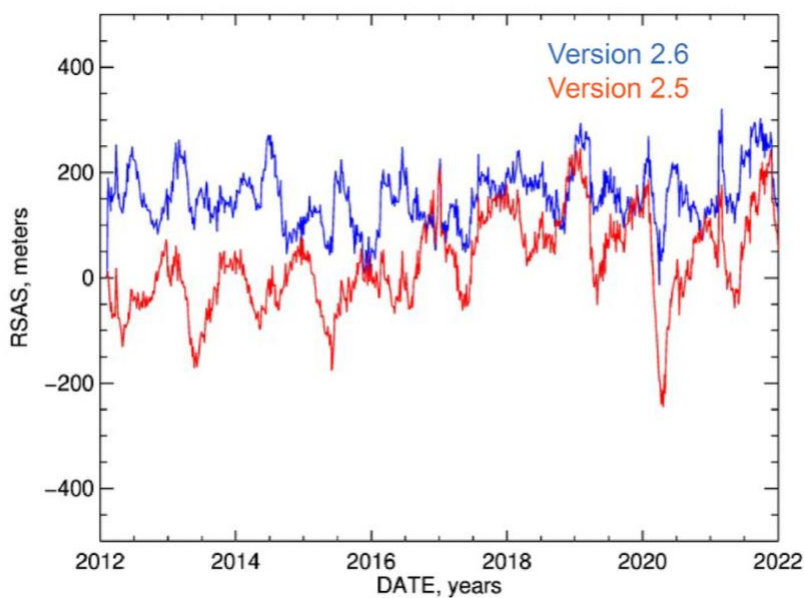
210 Two internal methods have been developed based on analysis of LP measured radiances
211 (Moy et al., 2017) to assess altitude registration independent of the spacecraft attitude information.
212 One method called Rayleigh scattering attitude sensing (RSAS), determines absolute altitude
213 errors using a ratio of radiances at 350 nm between 20 and 30 km and external knowledge of the
214 atmospheric pressure profile (Janz et al., 1996). The RSAS method is susceptible to inhomogeneity
215 in the underlying Earth scene and aerosol interference, which limits its application to longer time
216 scales and to regions and time periods with minimal aerosol contamination. The second method,
217 absolute radiance residual method (ARRM), looks at UV radiances shorter than ~ 305 nm at
218 altitudes between 60 and 65 km. These radiances have a sensitivity of 10% - 15% per 1 km
219 depending on the altitude and wavelength. The ARRM method is sensitive to errors in instrument
220 absolute calibrations, and therefore it is used primarily to evaluate relative errors in altitude
221 registration. The combined accuracy of the two altitude registration methods is about ± 200 m (Moy
222 et al., 2017).

223 In the v2.5 processing, four types of altitude corrections have been applied: a) static
224 correction (1.37 km for the center slit); b) 0.1 km jumps on 25 April 2013 to correct for a spacecraft
225 attitude system calibration change and on 5 September 2014 to account for observed attitude
226 changes; c) intra-orbital adjustments of up to 0.3 km in the center slit to account for image motion
227 at the focal plane; d) additional, seasonally varying intra-orbital altitude corrections of ~ 0.35 km
228 for the center slit, with the greatest adjustments during June and July. Absolute adjustments were
229 derived using the RSAS method while relative corrections (intra-orbital, inter-slit, and time-
230 dependent corrections) were based on ARRM results. After processing version 2.5 data, a 0.1-km
231 drift was detected by the RSAS method in sensor pointing (Kramarova et al., 2018). The
232 comparisons between LP version 2.5 and MLS ozone revealed a positive drift of $\sim 0.5\%/yr$ more
233 pronounced at altitudes above 35 km with the pattern consistent with a possible drift in sensor
234 pointing (Kramarova et al., 2018). The drift in version 2.5 ozone was also reported in other
235 independent studies (e.g. Wargan et al., 2020).

236 Over time we observed a divergence in results between the two altitude methods for SNPP
237 OMPS LP. We found unexpected drifts in the ARRM time series that differed for the 3 slits and
238 may be related to changes in instrument calibration at shorter UV wavelengths. Therefore, we
239 decided to not use the ARRM method for resolving the relative pointing of the three slits. In version
240 2.6 we updated all 3 types of corrections: static, intra-orbital, and time dependent. For the center

241 slit, the static correction now is 1.58 km (~ 0.2 km change from version 2.5). The intra-orbital
242 correction, still based on ARRM but simplified, now changes linearly as a fraction of orbit from
243 south to north. The correction is the same for the three slits, and the seasonal dependence is
244 removed. The image shift correction, the only correction not based on ARRM or RSAS, remains
245 unchanged. For the time-dependent correction, we left a single +0.1 km adjustment on 25 April
246 2013 to correct for the calibration adjustment that was acknowledged by spacecraft operators and
247 confirmed by other instruments on the SNPP platform. The second 0.1 km step on 5 September
248 2014, implemented in version 2.5, was removed. We found that this erroneous altitude correction
249 was the primary cause of the drift seeing in the LP version 2.5 ozone record. All sensor pointing
250 adjustments are applied to Level 1B measured radiances in version 2.6 processing.

251 Figure 1 shows the RSAS time series for the center slit. The 0.2 km offset between the two
252 versions is clearly seen at the beginning of the record, this is due to updates in the sensor's absolute
253 static pointing. The version 2.6 RSAS time series have smaller interannual variability due to
254 updated aerosol corrections and simplified seasonal pointing correction. The version 2.5 RSAS
255 has a clear upward drift by about +0.15 km over 10 years, which is not present in version 2.6. The
256 step in September 2014, now seen in version 2.6 RSAS, could be the result of spacecraft attitude
257 adjustment, but it is no different than similar steps such as in March 2019. There is no justification
258 to suspect these adjustments affect the long-term accuracy of the spacecraft attitude knowledge.



259
260 **Figure 1.** RSAS (Rayleigh Scattering Attitude Sensing) time series for versions 2.5 (red)
261 and 2.6 (blue) from April 2012 through December 2021 in the Southern hemisphere (50S-20S).

262 *The results are illustrated as errors in the instrument pointing expressed in meters. The RSAS*
263 *method is sensitive to aerosol interference therefore we limited the region to the southern mid-*
264 *latitudes where the LP measurement sensitivity to aerosol as well as aerosol contamination are*
265 *minimum. The Hunga eruption in January 2022 injected large amounts of aerosol into the*
266 *stratosphere and as a result substantially affected the RSAS record (see Sec. 2.2.5 and Fig. A9 in*
267 *Appendix).*

268

269 2.2.2 Version 2.6 LP Ozone Retrieval Algorithm

270 In version 2.6, we updated ozone and NO₂ absorption cross-sections and climatologies. In
271 the UV spectral range (295-355 nm), Brion-Dumont-Mallicet (BDM) (Brion et al., 1993) cross
272 sections provide more accurate ozone absorption coefficients at longer UV channels ($\lambda > 320$ nm)
273 compared to Bass and Paur (1985) cross-sections we used previously. BDM cross-sections are also
274 used by the ozone retrieval algorithms that derive ozone columns and profiles from the SNPP
275 OMPS nadir instruments (NM and NP). In the VIS range, Serdyuchenko-Gorshelev (SG) cross-
276 sections (Gorshelev et al., 2014) replaced those by Burkholder and Talukdar (1994). Nitrogen
277 dioxide (NO₂) cross sections from Mérianne et al. (1995) were replaced with those from Vandaele
278 et al. (1998) in version 2.6.

279 The retrieval algorithm needs ozone a priori profiles, and we use the updated seasonal ozone
280 climatology (Ziemke et al., 2021) in version 2.6 that is based on multi-year averaged MLS ozone
281 profiles in the stratosphere and model simulations with the Goddard Earth Observing System
282 (GEOS) Global Modeling Initiative (GMI) model in the troposphere. Previously, we used
283 McPeters and Labow (2012) climatology based on a set of MLS and sonde measurements. The
284 NO₂ climatology was constructed using the GEOS GMI model (Fisher et al., 2024). Since
285 stratospheric NO₂ concentration varies significantly during the day, the NO₂ climatology has an
286 additional dimension of local solar time (90 bins), in addition to 36 5-degree latitude bins and 12
287 seasonal bins. We discuss sensitivity of the LP ozone algorithm to changes in these parameters in
288 Sec. 2.2.4.

289 Aerosol attenuation affects ozone retrievals; therefore, we explicitly correct for this effect
290 using aerosol extinction profiles retrieved concurrently from the same OMPS LP measurements at
291 675 nm. To retrieve aerosol extinction profiles (Loughman et al., 2017) we need to assume an
292 aerosol particle size distribution. In version 2.6, we use the gamma-function particle size
293 distribution, which replaces the bimodal function used in version 2.5. Chen et al. (2018) has shown
294 improvements in retrieved aerosol at 675 nm after switching to the gamma-function distribution.

295 The radiance adjustment at ozone sensitive wavelengths is computed using the same gamma-
296 function particle size distribution.

297 Any clouds located along the LP line of sight shield the radiances scattered from lower
298 altitudes and reflect a large portion of the incoming radiation. The LP cloud detection algorithm
299 (Chen et al., 2016) uses the spectral dependence of the vertical gradient in radiance between two
300 wavelengths in the visible and near-IR spectral bands (674 and 868 nm) to discriminate between
301 clouds and aerosols. Once a cloud is identified we start ozone profile retrievals at an altitude 1 km
302 above the cloud top height.

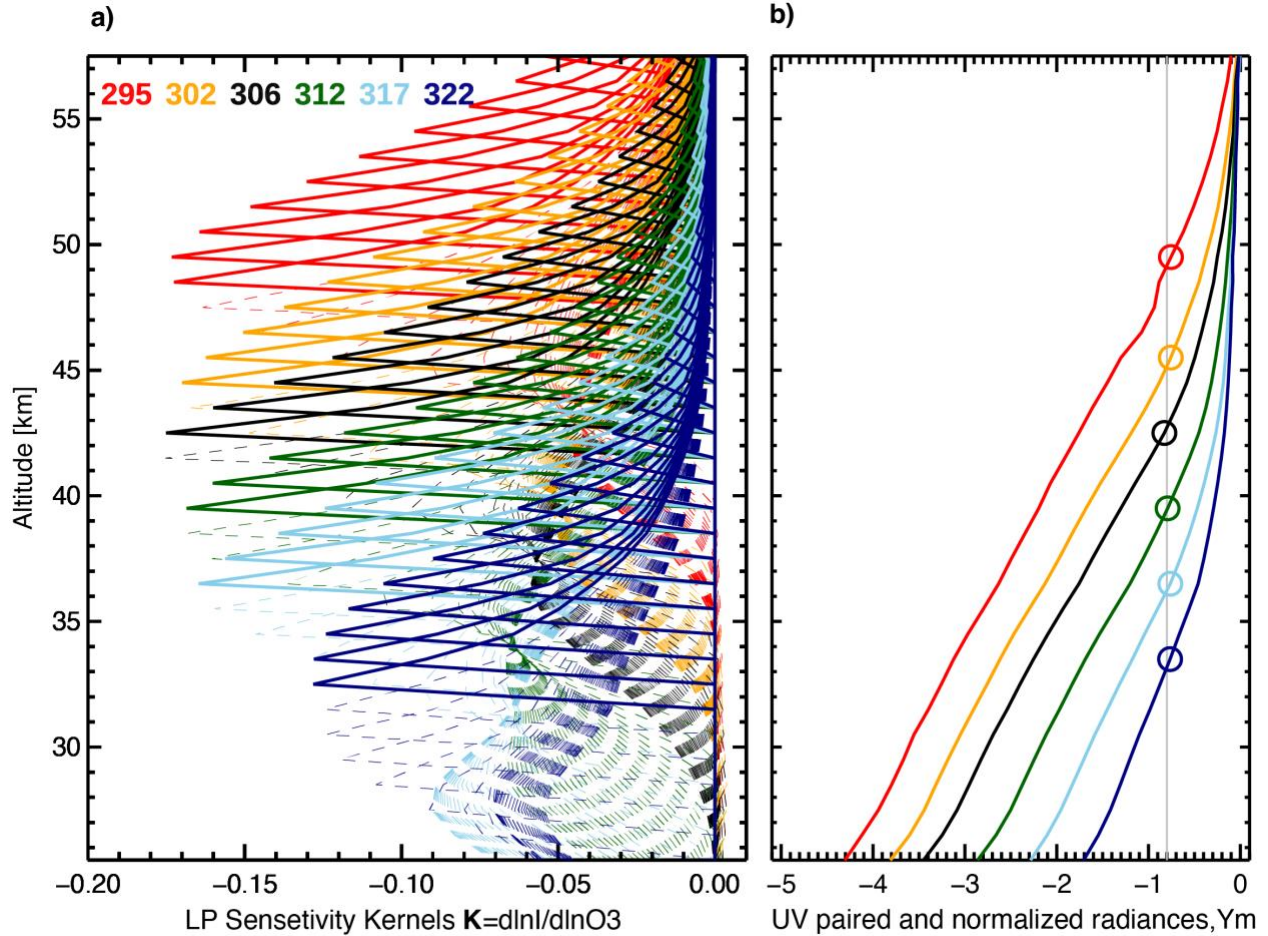
303 To simulate limb-scattered radiances in the forward model we use the Gauss-Seidel Limb
304 Scattering (GSLs) radiative transfer model (Herman et al., 1994; Loughman et al., 2005;
305 Loughman et al., 2015). Before simulating radiances, we first derive the scene reflectivity from
306 the LP measurements at 675 nm. If a cloud is detected, an effective surface reflectivity is computed
307 to represent a weighted average of the surface and cloud reflection, considering any clouds as
308 being present at the terrain height (Lambertian effective reflectivity approach).

309 In the ozone retrieval algorithm we use sun-normalized radiances when scattered radiances
310 are normalized by their solar irradiance counterparts to reduce the influence of spectral and
311 irradiance calibration errors (Jaross et al., 2014). To further minimize the sensitivity of the ozone
312 retrieval to absolute instrument calibration as well as to reduce effects of the underlying scene
313 reflectivity, and errors in the forward model, measured radiances are normalized with radiances
314 measured at high altitudes where sensitivity to ozone for a given wavelength is negligibly small
315 (Flittner et al., 2000). In version 2.6 algorithm, UV radiances are normalized at 60.5 km and VIS
316 radiances at 40.5 km. Ozone climatological profiles (Ziemke et al., 2021) are used to simulate
317 radiances at and above the normalization altitude. Climatological profiles are scaled at each
318 iteration based on retrieved ozone values from the previous iteration at altitudes 5 km below the
319 normalization altitude.

320 A key difference between this release and previous versions is that a single merged ozone
321 profile is retrieved using UV and VIS measurements between 12.5 km (or cloud top) and 57.5 km.
322 Ozone profiles in previous versions were retrieved independently from UV and VIS measurements
323 using wavelength pairs in the UV range and triplets in VIS (e.g. Rault and Loughman, 2013;
324 Kramarova et al., 2018). The version 2.6 algorithm uses radiances measured at six UV ozone-
325 sensitive wavelengths (295, 302, 306, 312, 317 and 322 nm) paired with 353 nm and one VIS

326 wavelength at 606 nm combined with 510 nm and 675 nm to form a triplet. The approach when
327 ozone-sensitive wavelengths are combined with the reference wavelength(s), which have almost
328 no ozone absorption, to form a pair or a triplet, minimizes the algorithm's sensitive to the
329 atmospheric pressure and temperature profiles used in the forward model calculations to simulate
330 radiances (Flittner et al., 2000). Wavelength pairs and triplets also help to reduce the sensitivity of
331 the retrieval algorithm to aerosols.

332 Each wavelength pair is used over a limited range of tangent point altitudes determined
333 from the vertical shape of sensitivity kernels and measured radiances (see Fig. 2). Limb scattered
334 radiances at ozone sensitive wavelengths first increase as they propagate to lower altitudes and
335 then reach the knee – a saturation when the radiances are not changing with altitude anymore (e.g.
336 Degenstein et al., 2009). Below the knee altitude, the UV channel become insensitive to changes
337 in ozone which is also reflected in decrease of the sensitivity kernels \mathbf{K} (Fig. 2a). We found that
338 the tangent altitude z where the sensitivity kernels \mathbf{K} start to degrade (Fig. 2a) corresponds to the
339 altitude where paired and altitude normalized radiances Y_m get smaller than -0.8 (Fig. 2b). The
340 vertical range for each pair is dynamic and changes from one profile to the next, but for the same
341 UV pair the range varies within 2-4 km (see Table S1, Supporting Information (SI)). We selected
342 UV pairs to maintain a near-constant sensitivity of the algorithm to changes in ozone over the
343 entire vertical range from 12.5 km to 57.5 km.



344

345 **Figure 2.** Left panel shows LP sensitivity kernels $dY(z,\lambda)/d\ln(O_3)$ for 6 UV pairs. Right
 346 panel shows vertical profiles of measured radiances normalized at 60.5 km and paired with the
 347 reference 353 nm wavelength. Colors represent different UV pairs. The vertical gray line indicates
 348 $Y = -0.8$ – the threshold used to cut UV pairs in the LP algorithm. Color circles show the lowest
 349 altitude where the given pair is used by the algorithm. Dashed lines on the left panel show that
 350 kernels below the lowest altitude used for each pair have decreasing magnitudes.

351

352 The version 2.6 algorithm uses the optimal estimation framework (Rodgers, 2000; Rault
 353 and Loughman, 2013) to iteratively retrieve ozone profiles X :

$$354 \quad X_{i+1} = X_i + (S_a^{-1} + R^T R + K^T S_\epsilon^{-1} K)^{-1} [(S_a^{-1} + R^T R)(X_a - X_i) + K^T S_\epsilon^{-1} (Y - F(X_i))] \quad (1)$$

355 Where i is the index that indicates the i^{th} iteration, X_a – a priori climatological ozone
 356 profile, S_a – a priori covariance matrix constructed as a diagonal matrix with the diagonal elements
 357 equal to the square of the a priori ozone values at that altitude $S_a(k,k) = X_a^2(k)$; S_ϵ – measurement
 358 noise covariance matrix is a diagonal matrix with the prescribed 1% noise for UV pairs. For the
 359 VIS triplet, noise is 0.5% for 27.5 km and below and gradually increases above 27.5 km reaching

360 1% at 37.5 km. The measurement vector \mathbf{Y} consists of 6 UV pairs and one VIS triplet. The GSLS
 361 radiative transfer model is employed to simulate radiances $F(\mathbf{X}_i)$ using a retrieved ozone profile
 362 from a previous iteration (or ozone climatological profile \mathbf{X}_a). $\mathbf{K}=\partial\mathbf{Y}/\partial\mathbf{X}$ is a matrix of weighting
 363 kernels (or Jacobian) each element of which represents the partial derivative of measurement
 364 vector \mathbf{Y} to a state vector \mathbf{X} (see also Fig. S1, SI). The weighting kernels \mathbf{K} are calculated by the
 365 GSLS forward model and updated after each iteration. In version 2.6, we use the second order
 366 Tikhonov's regularization (term \mathbf{R} , Livesey et al., 2006; Rault and Loughman, 2013) to improve
 367 stability of the ozone retrievals and to obtain the vertical resolution of ~ 2.0 km for ozone retrievals
 368 \mathbf{X} across all altitudes. The vertical resolution of LP ozone profiles is $\sim 1.9 - 2.5$ km between 20-55
 369 km, degrading to $\sim 3-8$ km at lower and higher altitudes. We use the Levenberg-Marquardt method
 370 to solve eq. 1 which helps finding solution for the non-linear problem by reducing the step between
 371 iterations.

372 2.2.3 Quality Flags in Version 2.6 Processing

373 The accuracy of LP retrieved ozone profiles depends on the combination of many
 374 individual factors. We report a set of quality flags to data users for filtering OMPS LP ozone
 375 retrievals. The algorithm runs a convergence test to determine when the iterations can be stopped
 376 using the following equation (Rodgers, 2000):

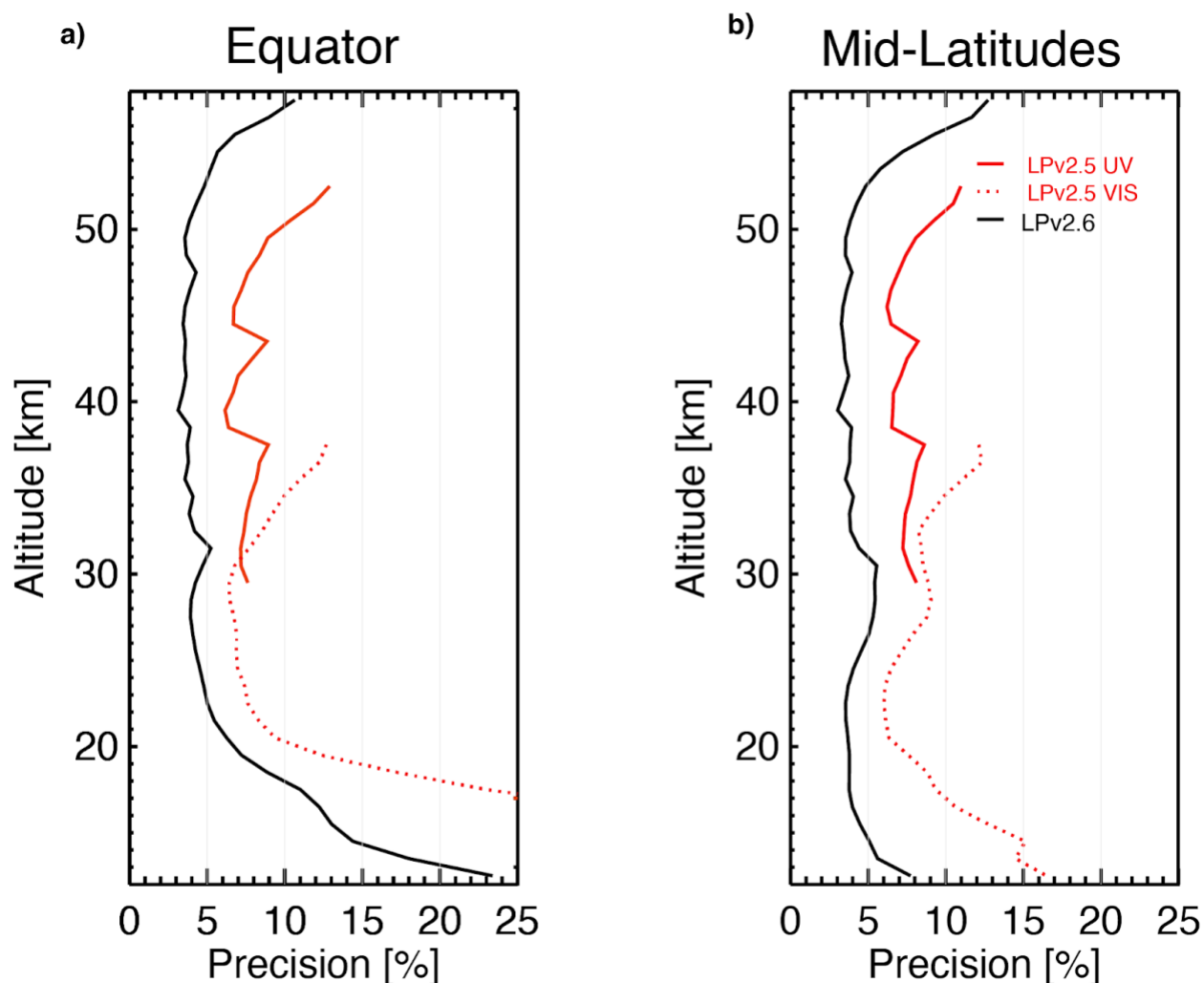
$$377 \quad d_i^2 = (\mathbf{X}_i - \mathbf{X}_{i-1})^T \hat{\mathbf{S}}^{-1} (\mathbf{X}_i - \mathbf{X}_{i-1}) \quad (2)$$

378 where d_i^2 is a convergence criterion after i^{th} iteration and $\hat{\mathbf{S}}$ is the solution covariance
 379 matrix defined as:

$$380 \quad \hat{\mathbf{S}} = (\mathbf{S}_a^{-1} + \mathbf{R}^T \mathbf{R} + \mathbf{K}^T \mathbf{S}_\epsilon^{-1} \mathbf{K})^{-1} \quad (3)$$

381 The iterations are stopped when the convergence criterion reduces with iteration ($d_i^2 < d_{i-1}^2$)
 382 and gets smaller than 10 ($d_i^2 < 10$). If after 7 iterations these conditions are not met, we assume
 383 that the retrieval did not converge and was not successful. Fewer than 1% of profiles have
 384 convergence values $d_i^2 > 10$ after 7 iterations. Typical number of iterations varies between 2 and 7.
 385 Users are thus recommended to use only profiles with the number of iterations (variable O3Status)
 386 ranging from 2 to 7 (inclusive) and the convergence less than 10 (variable O3Convergence).

387 The estimated precision for each profile retrieval is calculated using the square roots of
 388 diagonal elements of the solution covariance matrix \mathbf{S} (from eq. 3 above). Precision values range
 389 between 3-4% at altitudes between 20 and 52 km (Fig. 3). Larger precision values occur in the
 390 tropical upper troposphere and lower stratosphere (UT/LS) and in the mesosphere above 50 km.



391
 392 **Figure 3.** Retrieval precision of OMPS LP ozone profiles in % for version 2.5 (red lines)
 393 and version 2.6 (black line) in the tropics (a) and mid-latitudes (b) on March 1, 2015, orbit 17307,
 394 events 110 [15.9N, 110.6E] and 136 [44.2N, 102.6E], respectively. In version 2.5 precision was
 395 systematically larger indicating lower confidence.

396
 397 The LP algorithm uses a predefined set of wavelengths. Occasionally, measurements at the
 398 required wavelengths are not available and the algorithm looks for the nearest available
 399 wavelength within ± 0.4 nm in the UV region and ± 2.0 nm in VIS from the nominal wavelength.
 400 The retrieved profile will be flagged (ozone quality flag) if the algorithm cannot find measurements
 401 within the defined range. Users are recommended to not use profiles with the quality flag set (i.e.,
 402 only use profiles with O3quality=0). Approximately 1% of retrieved profiles are flagged in this
 403 manner.

404 Polar Mesospheric Clouds (PMCs) form at altitudes of around 80-85 km over polar
405 latitudes ($> 50^\circ$) in the summer months. PMCs can affect limb measured radiances at tangent
406 altitudes as low as 50 km if the clouds are in the line of sight (LOS) of the LP instrument. PMCs
407 increase scattering, and the magnitude of the excess signal produced by PMCs is greater in the NH
408 because PMC particles have an increased phase function in forward-scattering geometry (DeLand
409 and Gorkavyi, 2020). This excessive scattering by PMCs can lead to an underestimation of ozone
410 concentration, which we typically see in the upper portion of ozone profiles (above 35 km). We
411 identify PMC events by analyzing limb radiances at altitudes above 60 km and flag them in the
412 output files. This flag more often occurs in the Northern hemisphere (see Fig. 4a). We recommend
413 users to not use profiles affected by PMCs (i.e., only use profiles with `pmcflag=0`). The PMC flag
414 eliminates about 4-4.5% of data during summer months in both hemispheres (see also Fig. S2, SI).

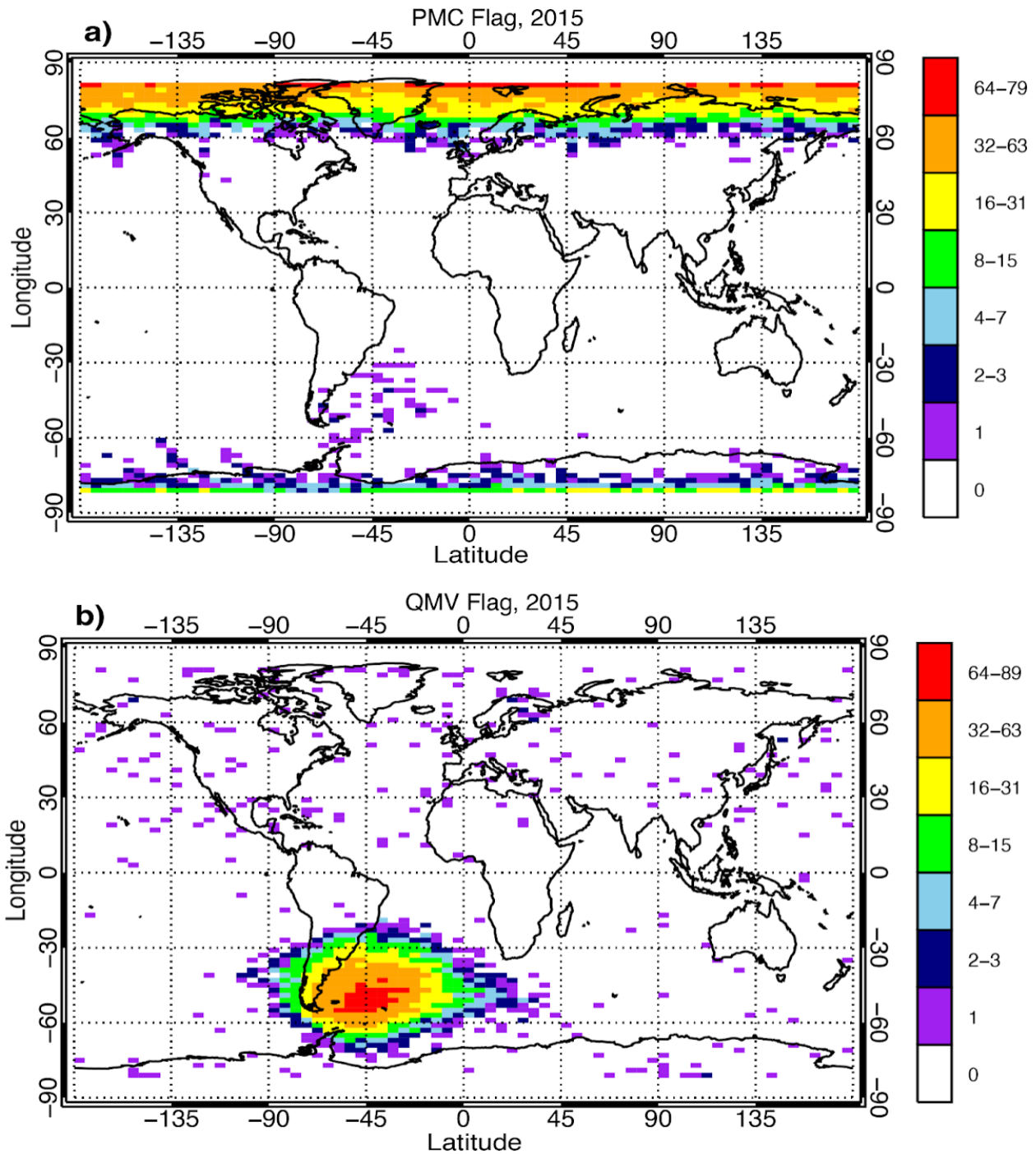
415 The retrieval algorithm aims to minimize the differences between measured and simulated
416 radiances. After the algorithm converges, we simulate radiances again using the retrieved ozone
417 profile. If the differences between simulated and measured radiances are still larger than the
418 assumed measurement noise (Kramarova and DeLand, 2023), we flag those retrievals using the
419 quality measurement vector (QMV) flag. The QMV flag eliminates about 2-2.5% profiles,
420 including cases when the measurements are affected by charged particles. We therefore
421 recommend removing any profile where the QMV flag is not equal to zero. Contamination of LP
422 radiance measurements by charged particles happens regularly when the satellite flies over the
423 South Atlantic Anomaly (SAA) region (see Fig. 4b), but occasionally, it also happens outside that
424 region. Any pixel on the LP CCD detector can be affected by charged particles, meaning that
425 measurements at any wavelength and at any tangent altitude can be compromised. The frequency
426 of the QMV flag does not vary seasonally or over the time of the SNPP mission (see also Figs. S3-
427 S4, SI), which is consistent with the majority of radiance anomalies having resulted from SAA
428 transients.

429 For scientific applications, we highly recommend using all these flags to filter out ozone
430 retrievals with lower quality. Accept profiles with the following parameters:

- 431 • The convergence criterion d^2 less than 10 (`O3Convergence < 10`);
- 432 • The number of iterations ranging between 2 and 7 inclusively (`2 < O3Status < 7`);
- 433 • No PMC contamination (`ASI_PMCflag=0`);
- 434 • Final residuals are smaller than assumed measurement noise (`QMV=0`);

435

- Measurements at all required wavelengths are available (O3Quality=0).



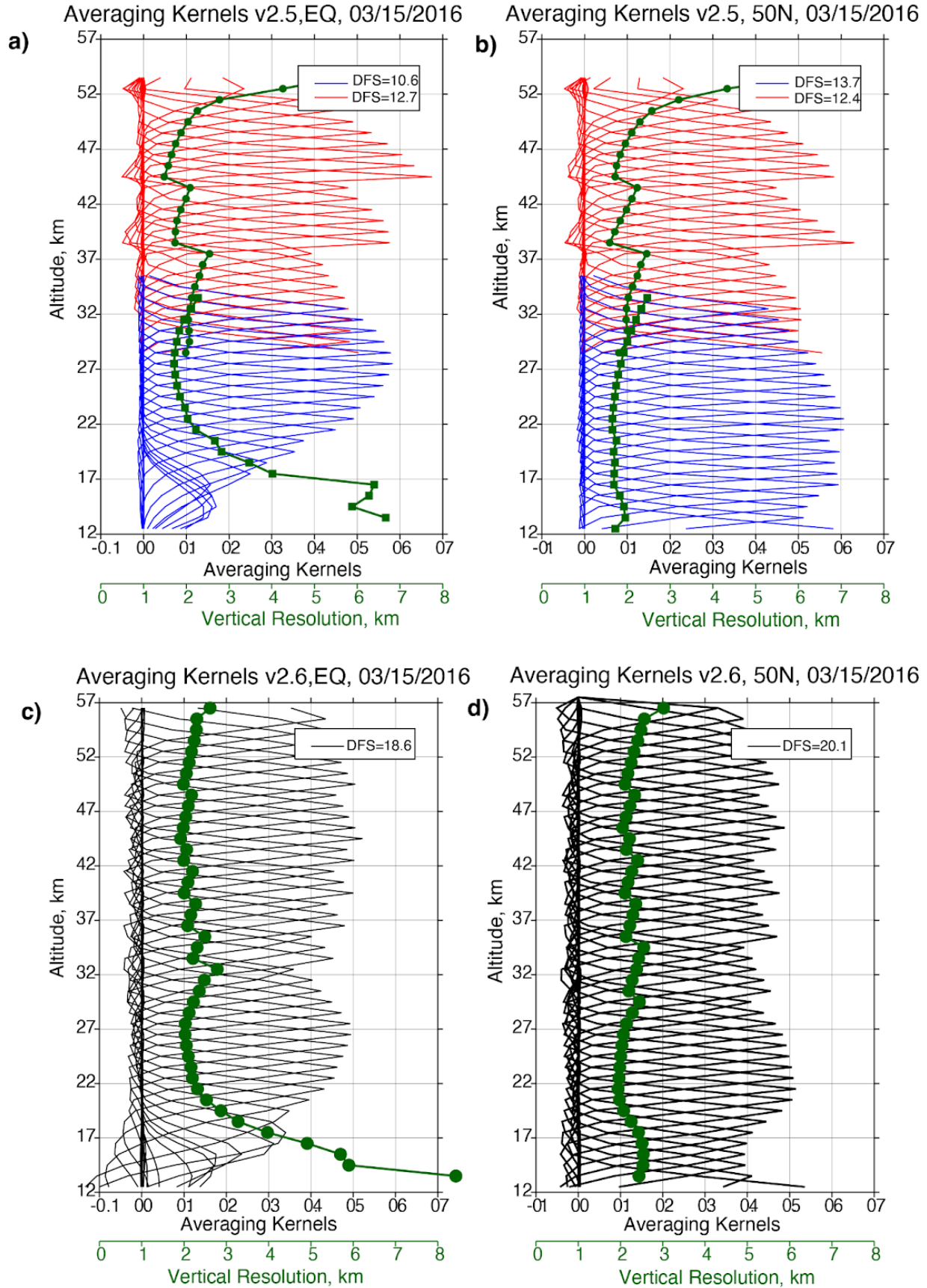
436

437 **Figure 4.** Spatial distribution of the PMC (a) and QMV (b) flags in 2015. The data are
 438 shown for 5 by 2 degrees spatial bins (longitude x latitudes) and expressed as the total number of
 439 profiles illuminated by the PMC (a) or QMV (b) flag in 2015. Increased flagging occurs south of
 440 the geographic location of the SAA because the tangent points are 3000 km distant from the
 441 satellite.

2.2.4 Analysis of Algorithmic Characteristics

In this section we discuss the version 2.6 algorithm performance. Averaging kernels are important components of the retrieval algorithm that characterize its sensitivity to true ozone changes. Version 2.6 averaging kernels are more consistent throughout the entire stratosphere (see Fig. 5c-d), while version 2.5 kernels (Fig. 5 a-b) sharply decrease at altitudes where the algorithm switches wavelengths. The combination of additional wavelengths and regularization applied in the version 2.6 algorithm improved consistency of the averaging kernels in terms of the peak magnitude and the width. The version 2.6 algorithm is able to maintain a uniform sensitivity throughout the entire vertical range. Using averaging kernels, we estimate that the degrees of freedom for the signal in version 2.6 is around 18-20. The vertical resolution of retrieved ozone profiles can also be estimated from averaging kernels (Rodgers, 2000) as the inverse of the diagonal elements of the averaging kernel matrix. The vertical resolution (Fig. 5 and also Fig. S5, SI) in version 2.6 ranges between 1.9-2.5 km, and is slightly degraded compared to the 1.7-2.0 km vertical resolution in version 2.5 (Kramarova et al., 2018). In the tropics the algorithm sensitivity below the ozone peak (below ~ 20 km) drops sharply (Figs. 5 a and c) leading to the vertical resolution of only 4-10 km in the lowermost tropical stratosphere and upper troposphere (12-20 km).

The algorithm sensitivity to the apriori can be also estimated using the averaging kernels (Rodgers, 2000). The LP ozone retrieval algorithm is very insensitive to apriori (see Fig. S6, SI) between 17 and 52 km in mid-latitudes and about 22-52 km in the tropics (Arosio et al., 2022). Sensitivity to apriori increases at the upper (above 52 km) and lower portion (below 17 km in mid-latitudes and 22 km in the tropics) of the profile where sensitivity of the LP measurements to ozone sharply declines.



466 **Figure 5.** Typical LP averaging kernels and vertical resolution in the tropics (a and c) and
467 in mid-latitudes (b and d). Panels (a) and (b) show version 2.5 kernels for UV (red) and VIS (blue)
468 retrievals, and the vertical resolution is shown in green with additional X-axis scale. Total degrees
469 of freedom for the signal, calculated as the sum of diagonal elements, are shown on the labels.
470 Panels (c) and (d) show kernels and vertical resolution for the same events from version 2.6
471 (March 15, 2016, orbit 22696, events 91 and 136, respectively).
472

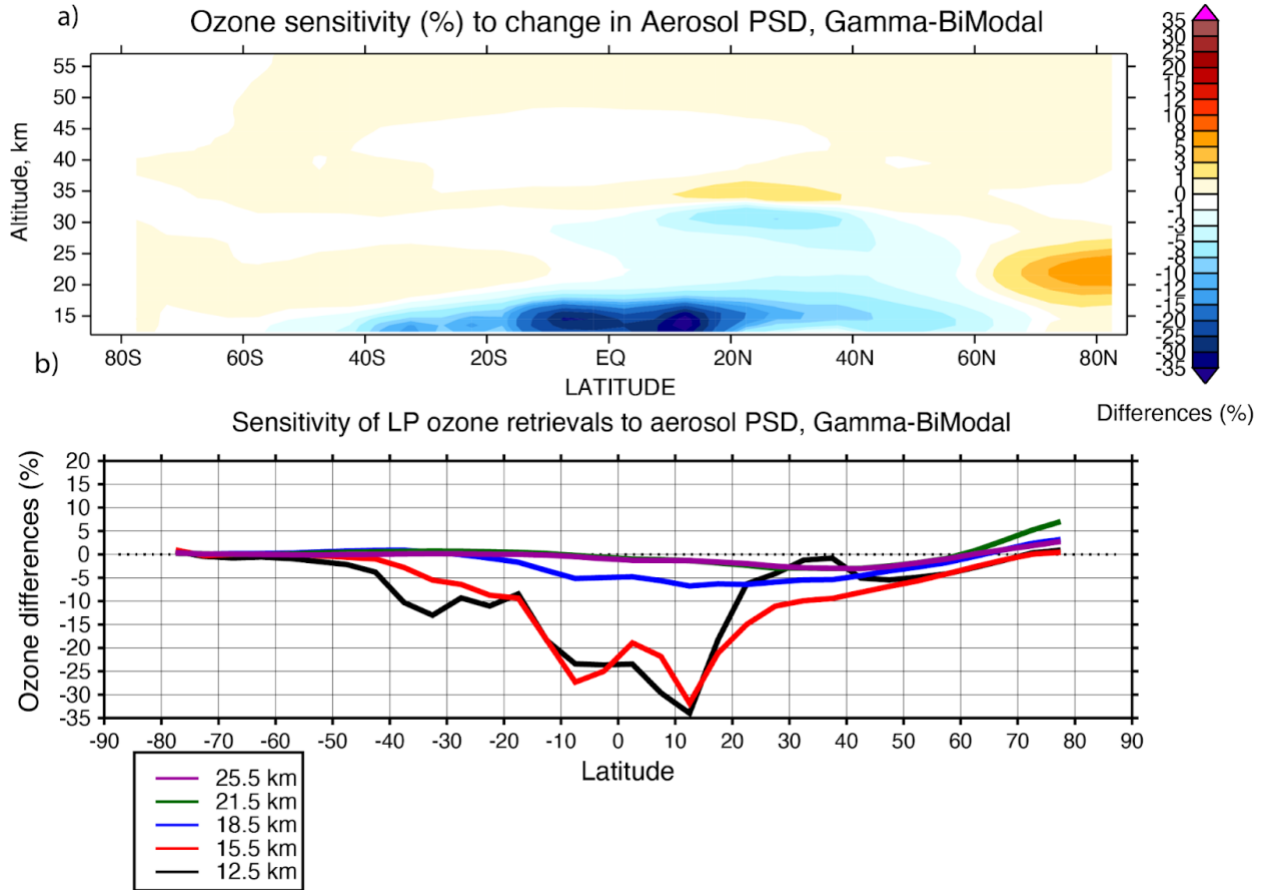
473 To estimate the algorithm sensitivity to changes in algorithmic parameters, such as the
474 replacement of ozone and nitrogen dioxide absorption coefficients, updates in ozone and nitrogen
475 dioxide climatologies, and changes in aerosol particle size distribution, we ran a series of tests in
476 which we replaced one parameter at a time and retrieved ozone for a day. We calculated responses
477 in ozone retrievals as differences between standard version 2.6 and the test with the perturbed
478 parameters. It is important to note that the aim of these was not to explain differences between
479 versions 2.5 and 2.6, but rather to evaluate sensitivity of the version 2.6 algorithm to changes in
480 these parameters. We found that replacement of nitrogen dioxide (NO₂) cross sections from
481 (Mérieulle et al., 1995) to (Vandaele et al., 1998) resulted in about 0.5-1% decrease in retrieved
482 ozone in the altitude range between ~ 32-36 km. This is due to increasing NO₂ absorption at longer
483 UV wavelengths (322 nm pair), which are used by the LP algorithm in this altitude range, and NO₂
484 concentration also peaks around 30 km (see Fig. S7, SI). In the second test, we estimated how the
485 replacement of the NO₂ climatology from the PRATMO (PRather ATmospheric Model)
486 photochemical box model (Prather and Jaffe, 1990; Brohede et al., 2007) to CEOS GMI (Nielsen
487 et al., 2017; Orbe et al., 2017) affected retrieved ozone. This switch in NO₂ climatology produced
488 almost no change in retrieved ozone above 30 km (<0.2%), but produced a small negative bias of
489 ~-0.5% below 30 km, particularly in mid-latitudes in both hemispheres (see Fig. S7, SI).

490 The replacement of ozone cross-sections from Bass and Paur (1985) in the UV and
491 Burkholder and Talukdar (1994) in the VIS to Brion-Dumont-Mallicet (BDM) (Brion et al., 1993)
492 and Serdyuchenko-Gorshelev (SG) (e.g. Gorshelev et al., 2014), respectively, produced systematic
493 differences in ozone retrievals, particularly above 30 km. Retrievals that use BDM cross-sections
494 yielded 1-2% larger ozone concentrations between 30 and 48 km, and reduced ozone above 50 km
495 by ~-0.5%. Below 30 km ozone slightly increased by ~0.5-0.8% (see Fig. S7, SI).

496 The switch in ozone climatology used as apriori produced almost no changes in retrieved
497 ozone profiles between 22 and 52 km in the tropics and between 17 and 52 km outside the tropics.
498 This is because the LP algorithm is not sensitive to apriori. However, we found small oscillations

499 of ± 0.2 -2% in the ozone differences when we changed ozone climatologies, but these oscillations
500 have a narrow 1-km width (see Fig. S7, SI). The retrieval algorithm behaves as a low-frequency
501 filter, and any fine scale structures either in the measurements or a priori that are finer than the
502 vertical resolution can not be retrieved. Therefore, it is very important to have smooth a priori
503 profiles without any sharp vertical gradients. We found that the ozone climatology used in version
504 2.5 had sharp vertical gradients and was responsible for vertical oscillations in the test results (see
505 Fig. S8, SI). Overall, updates in these four algorithmic parameters produced very small (less than
506 ± 1 -2%) but systematic changes in ozone retrievals.

507 We observed much larger changes in ozone retrievals (Fig. 6) after switching the assumed
508 aerosol particle size distribution from bimodal (Loughman et al., 2018) to gamma-function (Chen
509 et al., 2018). The ozone retrievals are corrected for aerosols using the aerosol extinction coefficient
510 profile derived from concurrent aerosol observations at 675 nm retrieved from the same LP
511 measurements. The radiance adjustment at ozone sensitive wavelengths is computed using the
512 assumed particle size distribution. The largest negative changes in ozone retrievals occur in the
513 tropical lower stratosphere and upper troposphere (below ~ 22 km), where changes can reach up
514 to 35% in 12.5-15.5 km range (Fig. 6). The sensitivity of the LP measurements to aerosols is very
515 weak in the Southern hemisphere, due to the aerosol phase function being much smaller in the
516 back-scattering direction that LP measures. Therefore, changes are very small in the southern mid-
517 and high latitudes (less than ± 1 %). In the northern subtropics, mid- and high-latitudes, sensitivity
518 to aerosol is much stronger, resulting in larger differences in the retrieved ozone due to the change
519 in assumed aerosol particle size distribution (Fig. 6). We see negative changes (up to -5%) in the
520 northern subtropics and mid-latitudes (EQ-55N) between 20-32 km, and positive changes (up to
521 3-8%) at high latitudes (60N-82N). The changes are very small above 32 km where the algorithm
522 uses UV measurements, and the concentrations of background stratospheric aerosols are typically
523 very low.



524

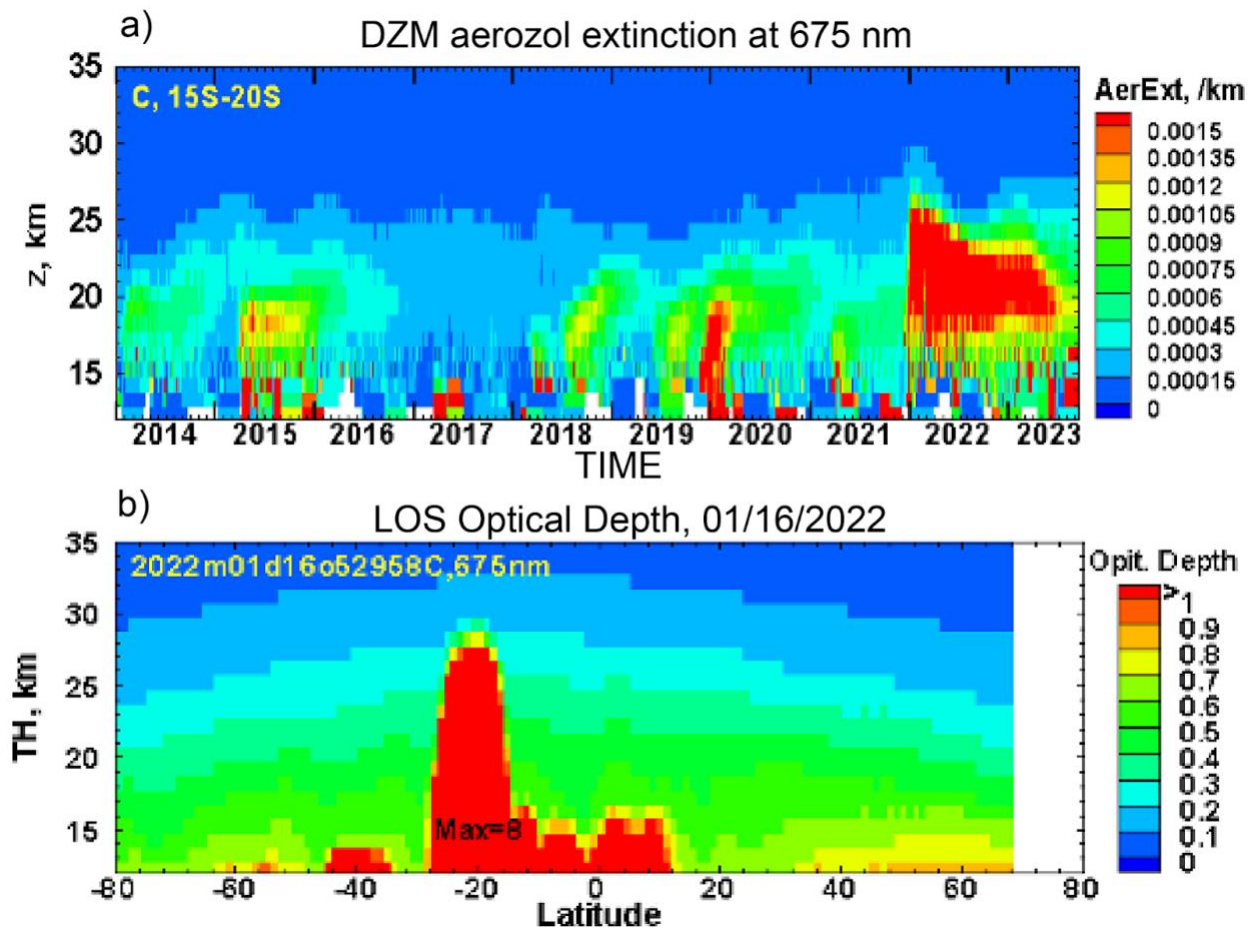
525 **Figure 6.** Sensitivity of the LP algorithm to a change in the aerosol particle size
 526 distribution from bimodal to gamma-function, which is equivalent to the change in aerosol models
 527 between versions 2.6 and 2.5. The upper panel (a) shows daily zonal mean differences in percent
 528 (note that the color scale is non-linear) as a function of latitude and altitude. The lower panel (b)
 529 shows daily zonal mean differences as a function of latitude for 5 levels in the lower stratosphere
 530 between 12.5 km and 25.5 km.

531

532 2.2.5 Effect of the Hunga volcanic aerosols on LP Ozone Retrievals

533 The explosive eruption of the Hunga volcano on 15 January 2022 injected aerosols and
 534 water vapor into the stratosphere and substantially increased stratospheric aerosol optical depth
 535 (Taha et al., 2022). Volcanic material has been detected at altitudes as high as 58 km shortly after
 536 the eruption which has never been observed during the satellite era. For several months
 537 immediately after the eruption, the aerosol concentration was very high, exceeding $1.5 \times 10^{-3} \text{ km}^{-1}$
 538 at altitudes up to 27 km near the ozone density peak (Fig. 7a). The total optical depth at 675 nm,
 539 integrated along the line of sight, was greater than 8 for one orbit the day after the eruption (Fig.
 540 7,b). The volcanic aerosol increased scattering, leading to sharp increases in LP radiances. The
 541 increased aerosol burden compromised the RSAS technique which we use to monitor the

542 instrument pointing (Fig. S9, SI). For several months, the LOS optical depth was greater than 1 at
 543 tangent altitudes near the ozone peak (23-26 km), making ozone retrievals impossible below 20-
 544 25 km. To eliminate profiles affected by volcanic aerosol we use retrieved aerosol extinction
 545 profiles at 675 nm. If retrieved extinction at 675 nm is greater than $1.5 \times 10^{-3} \text{ km}^{-1}$ at any altitude
 546 above 18.5 km, we cut ozone retrievals at and below that altitude (retrieved ozone values are set
 547 to a fill value). As a result of this filtering, there are gaps in the LP ozone record in the lower
 548 stratosphere, (below 25 km) mostly in the tropics and SH mid-latitudes, for 12-18 months after the
 549 eruption (see Fig. S10, SI).



550

551 *Figure 7. Upper panel shows daily zonal mean values of aerosol extinction in SH*
 552 *subtropics (15-20S) over the SNPP mission. Typical background aerosol extinction is $\ll 10^{-3} \text{ km}^{-1}$,*
 553 *particularly above 15 km, but extinction increases after volcanic eruptions (e.g. Calbuco*
 554 *eruption in 2015) or mega wildfires (2019-2020 New Year Australian fires). The Hunga eruption*
 555 *injected aerosol to an unprecedented height and increased zonally averaged aerosol extinction in*
 556 *the stratosphere to levels $> 1.5 \times 10^{-3} \text{ km}^{-1}$. Lower panel shows LOS optical depth at 675 nm for one*
 557 *orbit (#52958) on January 16, 2022. The LOS optical depth was well above 1 in the region near*
 558 *the eruption (with the maximum estimated LOS depth ~ 8). Ozone retrievals are not possible at*
 559 *conditions when the LOS optical depth exceeds 1.*

560

561 As seen in Fig. 7a, the volcanic aerosol slowly descended in the second half of 2022 (e.g.
562 Taha et al., 2022; Schoeberl et al., 2023) and spread into mid- and high- latitudes in both
563 hemispheres. As the aerosol optical depth declines, the number of successful ozone retrievals in
564 the lower stratosphere increases.

565 **3 Evaluation of OMPS LP Ozone Profiles**

566 Ozone profile retrievals from OMPS LP were evaluated previously (Kramarova et al.,
567 2018) by comparing with independent satellite profile measurements obtained from the Aura
568 Microwave Limb Sounder (MLS), Atmospheric Chemistry Experiment Fourier Transform
569 Spectrometer (ACE-FTS) and Odin Optical Spectrograph and InfraRed Imaging System
570 (OSIRIS). The study found that the mean differences between LP version 2.5 and correlative
571 measurements are well within $\pm 10\%$ between 18 and 42 km meeting the instrument requirements
572 (Flynn et al., 2006) and in many places within $\pm 5\%$. A positive drift of $\sim 0.5\%$ yr was detected in
573 the LP ozone record against MLS and OSIRIS with the pattern consistent with a possible 100 m
574 drift in the LP sensor pointing.

575 In this paper we evaluate the version 2.6 ozone profile dataset over 10+ years and we limit
576 our evaluation to comparisons with Aura MLS. The goal is to document mean differences and
577 long-term drifts between the two OMPS LP versions (version 2.5 and 2.6) using MLS as a
578 reference. A complementary study will follow, and it will provide a comprehensive evaluation of
579 version 2.6 against a larger set of correlative satellite and ground-based observations.

580 **3.1 Correlative measurements**

581 The Aura MLS record started in August 2004, and overlaps for more than 11 years with
582 SNPP OMPS LP. The equatorial crossing time of SNPP and Aura are very similar, and on some
583 days (about once a month) the two orbits are perfectly co-located. The vertical resolution of the
584 MLS ozone retrievals in the stratosphere is 3 km and decreases to 5.5 km in the mesosphere. We
585 use the latest version 5 of MLS data (Livesey et al., 2022). For validation with the limb scattering
586 OMPS LP, we limited MLS data to daytime observations (solar zenith angle $< 89^\circ$); and we filtered
587 MLS data using criteria recommended by the MLS Team.

588 **3.2 Comparison Technique**

589 In this study, for comparisons between OMPS LP and MLS, our spatial and temporal
590 collocation criteria are the following: profiles should be within $\pm 2^\circ$ latitude from each other with

591 the distance between them less than 1000 km and the time difference within ± 5 hours. We analyze
592 ozone profiles on the LP native coordinate system (number density on altitude grid), which
593 requires unit conversion for MLS retrievals. MLS volume mixing ratio profiles were first
594 interpolated on the LP regular altitude scale using GEOS FPIT (Lucchesi, 2013) pressure profiles
595 reported with OMPS LP data. Then, these interpolated mixing ratio profiles were converted into
596 number densities using the GEOS FPIT ancillary pressure and temperature profiles. Since the LP
597 algorithm does not retrieve ozone below the cloud top, we cut matching MLS ozone profiles at the
598 cloud top altitude as well to avoid biases due to different sampling in cloudy and cloud-free
599 conditions. In this study, we do not account for small differences in the vertical resolution of the
600 instruments. We further binned matched LP and MLS profiles into 5-degree latitude bins. We
601 adopted the same methodology described in Kramarova et al. (2018) to calculate biases and drifts.

602 3.3. Results and Discussions

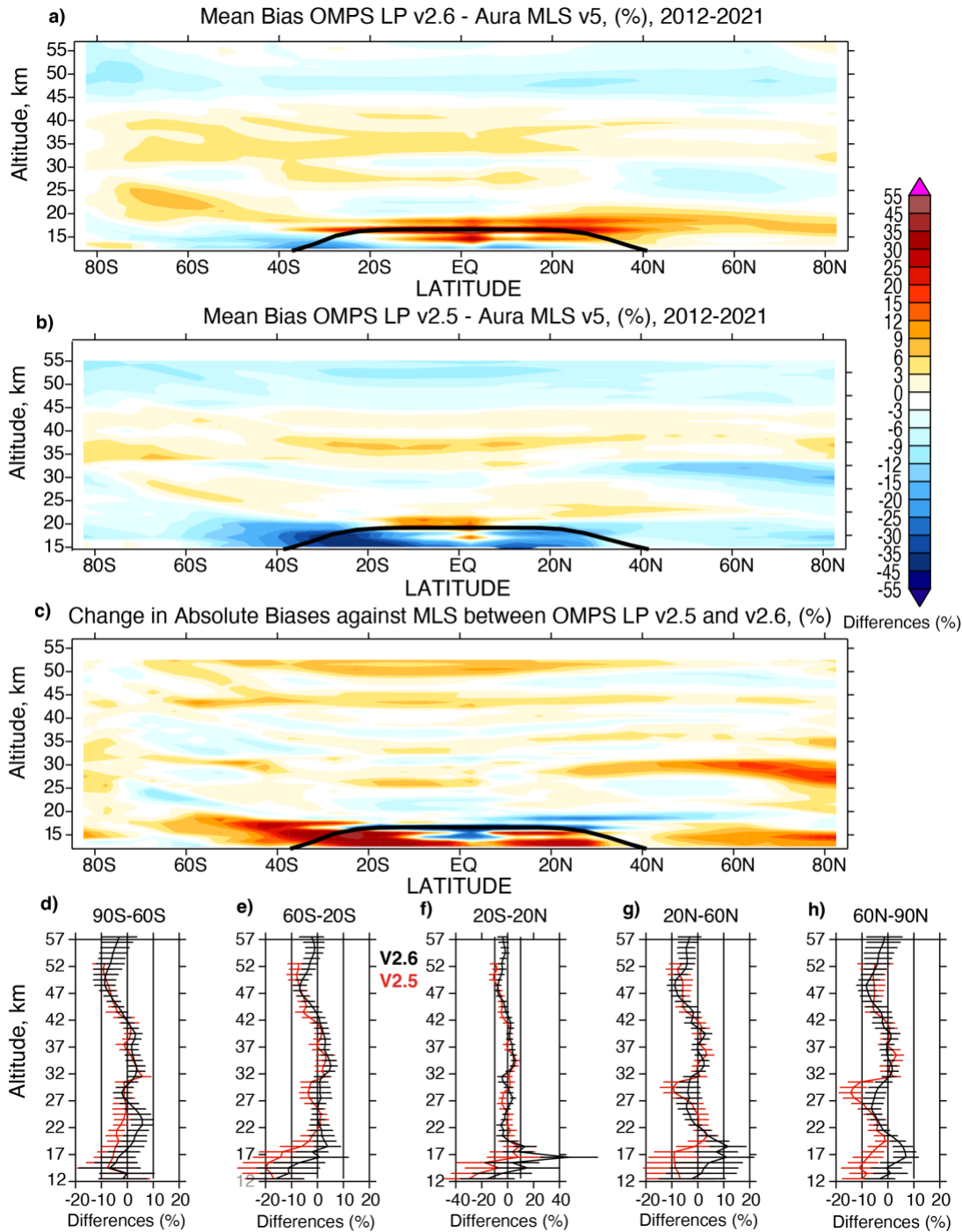
603 In this section we will compare two versions of OMPS LP – version 2.5 released in 2018
604 and version 2.6 released in 2023 - with MLS version 5. Our main goal is to highlight the major
605 differences between the two LP versions. Since version 2.5 data had not been screened for the
606 Hunga anomalies, we limit the time period for comparisons to April 2012 through December 2021.
607 In version 2.5, UV and VIS retrievals are done independently, so we use VIS retrievals between
608 12.5 km and 30.5 km and UV retrievals above 30.5 km.

609 The differences between the two LP versions are not large in the upper part of the profiles
610 above ~ 32 km (see Fig. 8). The biases between LP version 2.6 and MLS are mostly within $\pm 5\%$
611 between 20.5 and 45.5 km. Both versions exhibit positive biases relative to MLS on the order of
612 3-6% between 32 and 40 km, and negative biases above reaching -9% at ~ 48 km. In version 2.6,
613 biases with MLS decrease with increasing altitude above 48 km. The addition of three UV pairs
614 and increased normalization altitude (from 55.5 km to 60.5 km) in version 2.6 have resulted in the
615 extension of the upper limit of LP retrievals to 57.5 km. The increased number of wavelengths and
616 dynamic range, where each UV pair is used by the algorithm, have also helped to reduce the
617 oscillations seen in version 2.5 (Kramarova et al., 2018) at altitudes around 37.5 km and 43.5 km,
618 where the version 2.5 algorithm transitions between three pairs, and which are more apparent in
619 the southern hemisphere.

620 The differences between the two LP versions are larger in the lower part of the ozone
621 profiles below 31 km, where LP retrievals primarily rely on the VIS triplet (see Fig. 8). There are

622 many factors that contribute to this, including changes in ozone-sensitive wavelength in the VIS
623 triplet from 600 to 606 nm, aerosol particle size distributions, altitude registration and the stray
624 light correction. UV and VIS measurements are blended in the version 2.6 algorithm to provide a
625 smoother transition between 28 and 32 km. This effect is more pronounced in the North
626 Hemisphere, where version 2.5 shows strong negative biases between 25-30 km, as noted in the
627 previous study (Kramarova et al., 2018). These negative biases are still present in version 2.6 but
628 with a smaller magnitude of about -3 to -6%. Around 20 km there is a vertical band with strong
629 positive biases of about 5-20% in version 2.6 that extends from the southern midlatitudes (~40S)
630 to the northern polar latitudes that is not present in version 2.5. We found no changes in magnitude
631 or structure of the mean biases as we extended the time record up to the end of 2023 (see Fig. S11,
632 SI).

633 Another way to compare the two LP versions is to evaluate changes in absolute biases
634 against MLS between LP versions 2.5 and 2.6 (Fig. 8c): $|O_3^{LP2.5} - O_3^{MLS}| - |O_3^{LP2.6} - O_3^{MLS}|$.
635 Positive biases (redish colors) in Fig. 8c represent places where LP version 2.5 has larger absolute
636 biases against MLS compared to version 2.6, and therefore these are the places where the absolute
637 biases decreased in LP version 2.6. Noticeable improvements ($> \sim 5\%$), as we noted before, can be
638 seen in the North Hemisphere between 25-30 km, in the lowermost stratosphere and above 50 km.
639 But absolute biases increased in version 2.6 by more than 5% at 20 km from 40S-70N, between
640 25-20 km in the Southern mid-latitudes 50S-70S and in the equatorial upper troposphere.



641

642

643

644

645

646

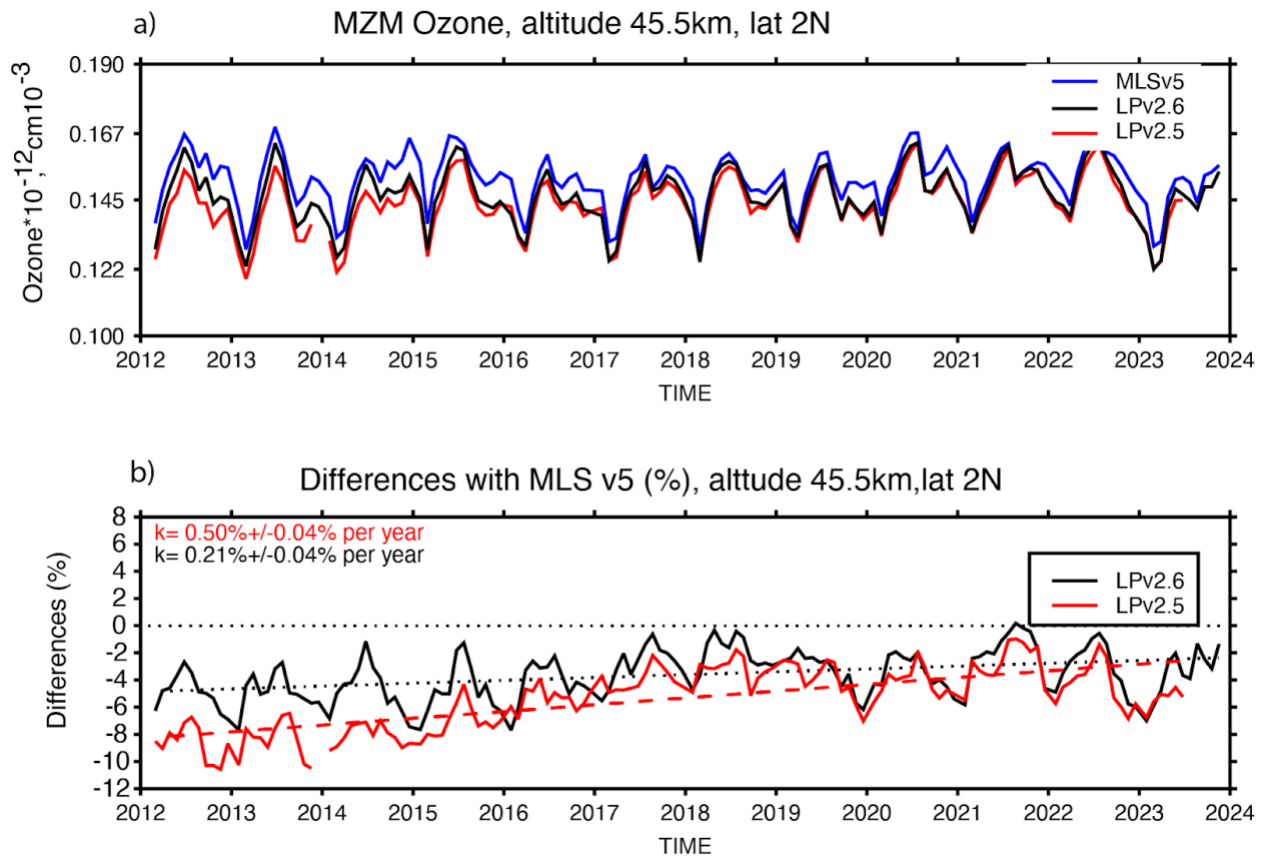
647

648

Figure 8. Mean biases between OMPS LP and MLS version 5 over 10 years between Apr. 2012- Dec. 2021. Panel (a) shows mean biases in percent (%) for version 2.6 of OMPS LP data as a function of altitude between 12.5 and 57.5 km and latitude (5-degree grid). The black solid line shows the mean tropopause height. Panel (b) is the same as panel (a) but for version 2.5. Panel (c) shows changes in (%) in absolute biases against MLS between versions 2.5 and 2.6, essentially differences between absolute values shown in panels (b) and (a). Panels(d-h) show biases between versions 2.6 (black lines) and 2.5 (red lines) against MLS in 5-degree wide latitude

649 bins. Horizontal lines represent 1 standard deviation for mean differences. The standard error of
 650 the mean is typically smaller than the width of the lines.

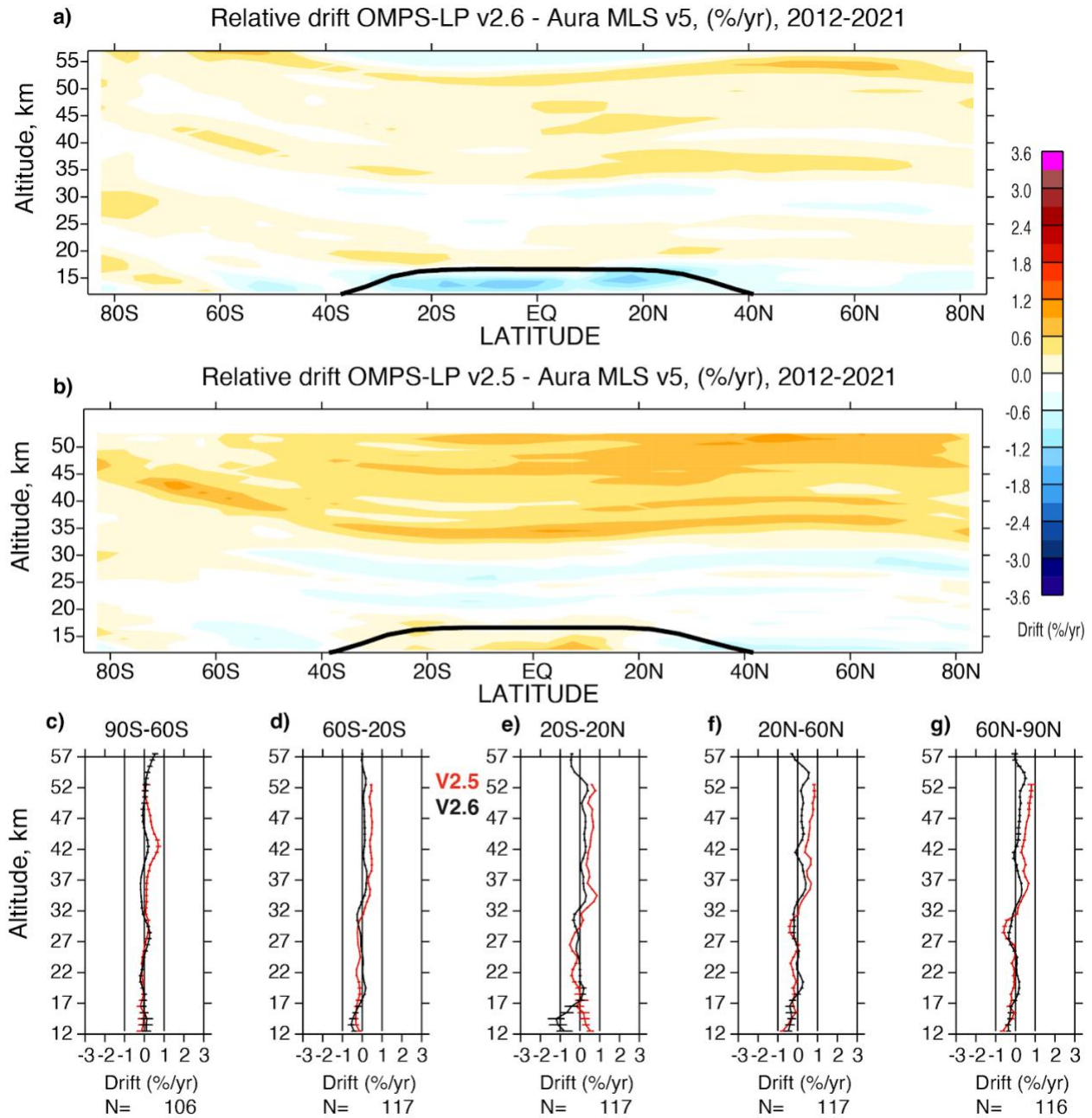
651 To investigate the stability of the LP record, we analyzed the MLS and LP ozone time
 652 series at each latitude and altitude grid (Figs. 9-10). Previously, in version 2.5, we found a
 653 significant upward drift at altitudes above 35 km, where ozone retrievals are very sensitive to the
 654 accuracy and stability of the instrument pointing. We found that the version 2.6 LP record is more
 655 stable, and compares better with MLS. There is a small upward drift between LP version 2.6 and
 656 MLS in early years between 2012 and 2018 (Fig.9), but after that there is no obvious drift. We
 657 believe that the removal of the second 0.1-km step in altitude registration in September 2014, and
 658 the time-dependent spectral shift corrections are responsible for the observed improvements. The
 659 mean negative offset is also smaller between version 2.6 and MLS, mostly due to the changes in
 660 the earlier part of the record (Fig. 9b).



661
 662 **Figure 9.** (panel a): LP and MLS time series of ozone number density at 45.5 km, where
 663 LP retrievals are most sensitive to the instrument pointing. (panel b): time series of differences
 664 (in%) between LP and MLS for versions 2.5 (red) and 2.6 (black). Dashed/dotted color lines show
 665 linear fits to differences. Differences between MLS and version 2.6 are smaller in 2012 by ~2%
 666 compared to differences with version 2.5. The relative drift against MLS has reduced from 5% per
 667 decade ($\pm 0.4\%$) in version 2.5 to 2.1% per decade ($\pm 0.4\%$) in version 2.6.

668

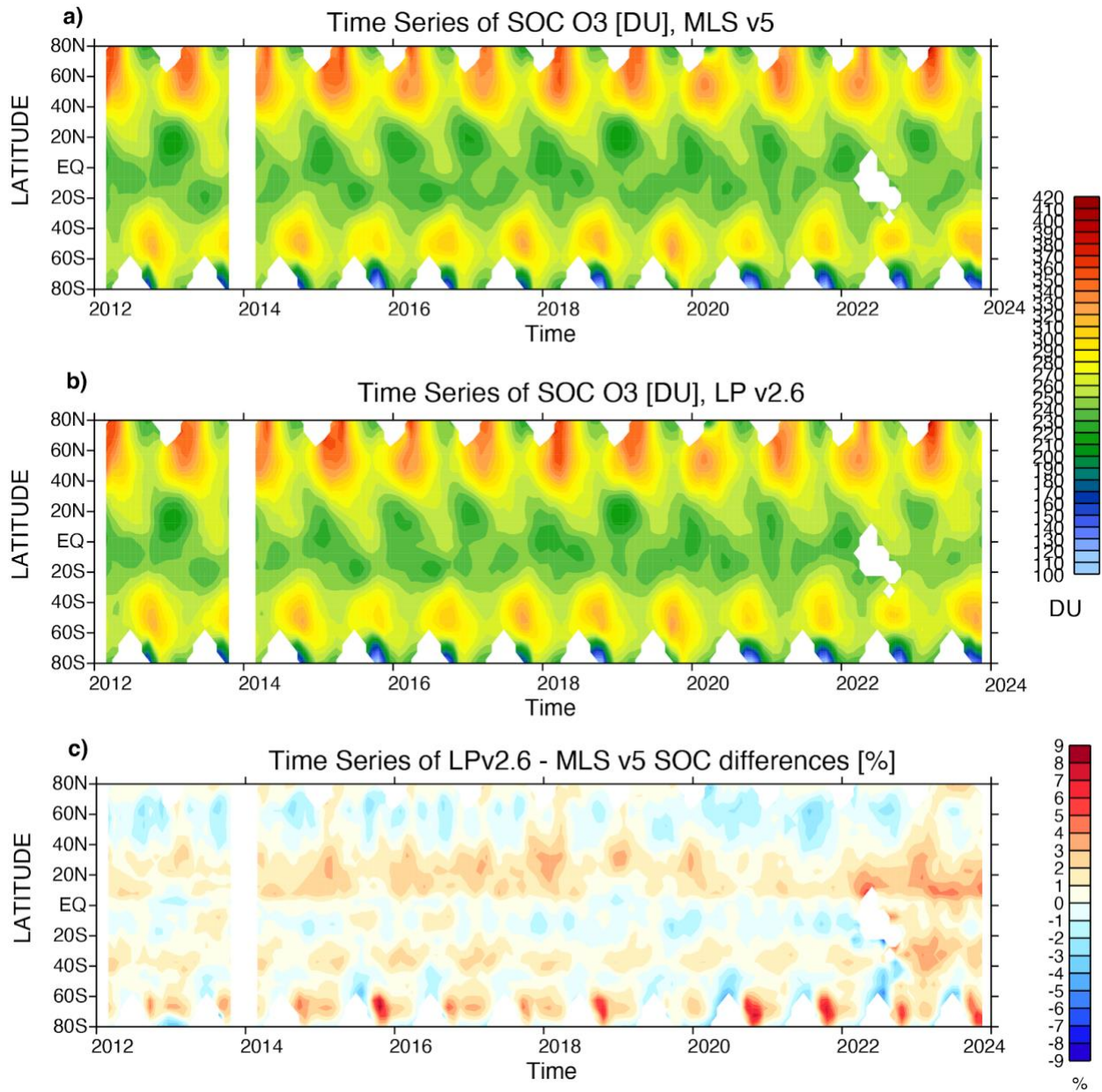
669 We estimated the relative drift between LP and MLS by simply fitting a linear trend to the
670 monthly zonal mean differences (Figs. 9b and 10). In version 2.5, the vertical pattern in the relative
671 drift (Fig. 10b) was consistent with a possible drift in altitude registration: the drift is
672 predominantly positive above the ozone peak and negative below. We found that the pattern is
673 very different in version 2.6 (Fig.10a). Overall, we see a substantial reduction in the magnitude of
674 the drift, making the version 2.6 record more suitable for the ozone trend studies. While the drift
675 between LP version 2.6 and MLS is still predominantly positive in the upper stratosphere, a
676 magnitude has reduced to about 0.2% per year (or 2% per decade) or less. We found that the
677 relative drift decreases in the upper stratosphere if we extend the considered time period by 2 more
678 years to the end of 2023 (see Fig. S12, SI). In the middle stratosphere between 25-35 km the drift
679 is slightly negative. We also see a strong negative relative drift in the upper equatorial troposphere
680 up to -10% per decade while it was positive in version 2.5. Though the record extension reduces
681 the drift in the upper stratosphere, the drift in the southern subtropics (20S-40S) between 15 and
682 21 km (see Fig. S12, SI) sharply increases suggesting that LP retrievals overestimate ozone
683 concentrations after the Hunga eruption in that region.



684

685 **Figure 10.** Panel a: relative drift between OMPS LP version 2.6 and MLS version 5 over
 686 almost 10 years from April 2012 through December 2021 as a function of altitude and latitude (5°
 687 latitude grid). Solid black line shows the mean tropopause height. Panel (b) is the same as panel
 688 (a) but for OMPS LP v2.5. Panels (c-g) show vertical structures of the relative drift in 5 wide
 689 latitude bins for versions 2.5 (red lines) and 2.6 (black lines). Horizontal error bars show 1σ errors
 690 for the linear fit. Numbers on the bottom indicate the number of months in each of the 5 bins.
 691

692 Finally, we consider the time series of stratospheric ozone columns (SOC) between 12.5
693 km and 57.5 km (Fig. 11). If LP ozone profiles were truncated because of the presence of clouds,
694 we cut the matching MLS profile as well and integrate profiles down to the lowest available level.
695 However, we require the minimum number of levels in the profile to be equal to 40 (corresponds
696 to 18.5 to 57.5 km). After the Hunga eruption we filtered LP profiles leading to a gap in the SOC
697 record in the equatorial latitudes. Both LP and MLS show similar latitudinal and seasonal patterns
698 in the SOC distribution suggesting that LP ozone can be used to extend MLS record into the future
699 for many applications. The differences range mostly to within $\pm 2\%$ but there are clear latitudinal
700 and seasonal patterns. The largest seasonal variations are observed over the southern polar
701 latitudes, with a strong positive bias observed during austral spring. It is outside of the scope of
702 this study to analyze seasonal differences, but this topic will be considered in the upcoming
703 comprehensive validation paper where OMPS LP will be compared with an extended set of
704 correlative satellite and ground-based observations. The differences in SOC increase in the last
705 two years and become predominantly positive in the tropics and mid-latitudes. The increases in
706 mean differences in 2022-2023 are more apparent at altitudes near the ozone peak between 22 and
707 26 km (see Fig. S13, SI). The Hunga eruption increased concentration of water vapor in the
708 stratosphere globally (e.g. Millán et al., 2022), but the LP wavelengths used by the retrieval
709 algorithm are not sensitive to water vapor absorption. Further investigation is needed to understand
710 these changes and any potential links to the Hunga eruption.



711

712 **Figure 11.** Time series of monthly zonal mean stratospheric ozone columns in DU
 713 derived from MLS version 5 (a) and OMPS LP version 2.6 (b) shown as a function of latitude
 714 and time. Stratospheric columns are integrated between 12.5 km or cloud top and 57.5 km. Panel
 715 (c) shows differences in % between LP and MLS.

716

717

4 Conclusions

718

719

720

721

In this study we described the new version (version 2.6) of OMPS LP ozone profile dataset. Overall, the new version 2.6 of the OMPS LP ozone profile dataset represents incremental improvements in calibration, retrieval algorithm, and data quality compared to the previous version 2.5. OMPS LP provides ozone profiles with a high vertical resolution and dense spatial sampling,

722 offering an adequate alternative for extending MLS ozone record into the future for many
723 applications. We described changes in calibration applied to measured limb-scattered radiances
724 and modifications implemented into the retrieval algorithm.

725 Calibration updates that affected ozone retrievals include improvements in the stray light
726 model, radiometric calibration, the wavelength shift correction and altitude registration. As a result
727 of updates in altitude registration, the RSAS technique, applied to the time period between April
728 2012 and December 2021, demonstrated improvements in the stability of the version 2.6 record
729 with no apparent trends.

730 The LP retrieval algorithm was also modified in version 2.6. Following recommendations
731 provided in the scientific literature, we replaced outdated algorithmic parameters such as ozone
732 and nitrogen dioxide absorption cross-sections and climatologies. Though these updates yield very
733 small systematic (less than $\pm 1-2\%$) changes in ozone retrievals, it is important to use the best
734 available parameters. In addition, we replaced the particle size distribution model for stratospheric
735 aerosols. We now use the gamma-function model to retrieve aerosol extinction from the same limb
736 measurements at 675 nm which are then used to correct for the aerosol contamination in the ozone
737 retrieval algorithm. We estimated the sensitivity of the algorithm to changes in the assumed
738 particle size distribution and show that the largest changes, up to 30-35%, are seen in the tropical
739 (20S-20N) upper troposphere (12.5-15.5 km), where the aerosol concentration is typically higher
740 and the LP sensitivity to ozone is low. In the middle stratosphere (18.5-30.5 km), the ozone
741 algorithm is more sensitive to changes in the aerosol model in the Northern hemisphere because
742 of the forward scattering geometry of the LP observations. The changes in the aerosol model there
743 can produce up to $\pm 2-7\%$ error in retrieved ozone.

744 The largest algorithmic change in version 2.6 is that we combine UV and VIS
745 measurements and retrieve a single merged ozone profile between 12.5 and 57.5 km. We also
746 increased the number of UV pairs to 6, increased the normalization altitude for UV radiances to
747 60.5 km, limited the vertical range where each UV pair contributes based on sensitivity to ozone,
748 and employed Tikhanov's regularization. We found that the averaging kernels are more consistent
749 throughout the entire profile in terms of the peak magnitude and the width. This means that the
750 version 2.6 algorithm is better optimized for keeping a uniform sensitivity throughout the entire
751 vertical range with the resolution of $\sim 1.9-2.5$ km. The vertical resolution quickly degrades in the
752 tropics below the ozone peak and decreases to 4-10 km between 12.5 and 17.5 km in the tropical

753 upper troposphere. The retrieval precision, reported with each profile, has reduced by a factor of
754 two compared to version 2.5 and ranges between 3-4% in the middle stratosphere. The accuracy
755 of LP retrieved ozone profiles depends on many factors, and we report a set of quality flags to help
756 users identify and exclude data with a lower quality. In this study, we introduced each flag and
757 analyzed their spatial and temporal distribution.

758 We compared the OMPS LP record with Aura MLS and found incremental improvements
759 in version 2.6. The algorithm modifications helped to reduce vertical oscillations seen in the
760 previous version, particularly near altitudes where the algorithm switches wavelengths. Negative
761 biases above 45 km have been reduced in version 2.6. Because UV and VIS radiances are merged
762 in the middle stratosphere, version 2.6 enables a smoother transition in the altitude range between
763 28 and 33 km. Mean biases with MLS are within $\pm 10\%$ above 20 km and in many places are less
764 than $\pm 5\%$.

765 The most notable improvement in version 2.6 is the reduction in relative drifts between LP
766 and MLS. Particularly, in the upper stratosphere above 35 km – the region most sensitive to error
767 in altitude registration – the relative drift between LP version 2.6 and MLS is around or less than
768 2% per decade (versus 5-10% for LP 2.5 - MLS).

769 We introduced a filter based on retrieved aerosol extinction to remove ozone profiles
770 affected by the Hunga eruption in the lower stratosphere (below 24.5 km). As a result of the
771 filtering, there are gaps in OMPS LP observations in the lower stratosphere between 12.5-22.5 km
772 in the southern midlatitudes and tropics (45S-20N) that last for several months following the
773 eruption. We see an increase in differences between LP and MLS in 2022-2023 compared to the
774 previous 10 years. Further investigation is needed to determine if the 2022-2023 increase is related
775 to the elevated stratospheric aerosol load due to the Hunga eruption.

776 Overall, the findings of this study demonstrate the importance of continuous improvements
777 in instrument calibration and retrieval algorithms to ensure high accuracy and stability of satellite
778 ozone measurements. Periodic evaluation of the LP ozone datasets, and comparisons with
779 independent measurements, are critical for determining the reliability and fitness of the LP data
780 for various scientific applications.

781 **Acknowledgments**

782 Authors are grateful to the MLS Team at NASA JPL for producing consistent high-quality
783 ozone dataset. Authors would like to thank Didier Rault for developing the original ozone retrieval

784 algorithm for the OMPS LP. We also would like to thank Robert Loughman for maintaining the
785 radiative transfer code for the OMPS LP. We are grateful to all members of the OMPS Team for
786 their work on supporting the OMPS mission. This work was funded under the NASA project 20-
787 SNPPSP20-0019 “Synergistic use of Limb and Nadir Measurements to continue the NASA
788 Standard Ozone Products from OMPS on Suomi NPP and NOAA-20”. SD and YJ were supported
789 by a NOAA JPSS Proving Ground and Risk Reduction Program grant. Authors would like to thank
790 Nigel Richards for constructive comments.

791 **Open Research**

792 Suomi OMPS LP ozone data available at:

793 https://disc.gsfc.nasa.gov/datasets/OMPS_NPP_LP_L2_O3_DAILY_2.6/summary

794 Natalya Kramarova (2023), OMPS NPP LP L2 Ozone Vertical Profile swath daily V2.6,
795 Center Slit, Greenbelt, MD, USA, Goddard Earth Sciences Data and Information Services Center
796 (GES DISC), accessed [April 5, 2024], doi:10.5067/8MO7DEDYTBH7.

797 Aura MLS data available at:

798 https://disc.gsfc.nasa.gov/datasets/ML3DBO3_005/summary

799 Schwartz, M., Froidevaux, L., Livesey, N., Read, W., and Fuller, R. (2021), MLS/Aura
800 Level 3 Daily Binned Ozone (O₃) Mixing Ratio on Assorted Grids V005, Greenbelt, MD, USA,
801 Goddard Earth Sciences Data and Information Services Center (GES DISC), Accessed: [April 5,
802 2024], [10.5067/Aura/MLS/DATA/3516](https://doi.org/10.5067/Aura/MLS/DATA/3516)

803 **References**

804 Arosio, C., Rozanov, A., Gorshchev, V., Laeng, A., and & Burrows, J. P. (2022).: Assessment of
805 the error budget for stratospheric ozone profiles retrieved from OMPS limb scatter measurements,
806 *Atmospheric Measurement Techniques* Atmos. Meas. Tech., 15, 5949–5967,
807 <https://doi.org/10.5194/amt-15-5949-2022>, 2022.

808 Bass, A. M., & Paur, R. J. (1985). The ultraviolet cross-sections of ozone: I. The Measurements.
809 In C. S. Zerefos, & A. Ghazi (Eds.), *Atmospheric Ozone* (pp. 606–616). Dordrecht: Springer.
810 https://doi.org/10.1007/978-94-009-5313-0_120

811 Brion, J., Chakir, A., Daumont, D., Malicet, J., & Parris, C. (1993). High resolution laboratory
812 absorption cross-section of O₃. Temperature effect. *Chemical Physics Letters*, 213, 610–612.
813 [https://doi.org/10.1016/0009-2614\(93\)89169-I](https://doi.org/10.1016/0009-2614(93)89169-I)

814 Brohede, S. M., Haley, C. S., Mclinden, C. A., Sioris, C. E., Murtagh, D. P., Petelina, S. V., et al.
815 (2007). Validation of Odin/OSIRIS stratospheric NO₂ profiles. *Journal of Geophysical Research:*
816 *Atmospheres*, 112(D7), D07310. <https://doi.org/10.1029/2006JD007586>

- 817 Burkholder, J. B., & Talukdar, R. K. (1994). Temperature dependence of the ozone absorption
818 spectrum over the wavelength range 410 to 760 nm. *Geophysical Research Letters*, 21, 581–584.
819 <https://doi.org/10.1029/93GL02311>
- 820 Chen, Z., Bhartia, P. K., Loughman, R., Colarco, P., & DeLand, M. (2018). Improvement of
821 stratospheric aerosol extinction retrieval from OMPS/LP using a new aerosol model. *Atmospheric*
822 *Measurement Techniques*, 11, 6495–6509. <https://doi.org/10.5194/amt-11-6495-2018>
- 823 Chen, Z., DeLand, M., & Bhartia, P. K. (2016). A new algorithm for detecting cloud height using
824 OMPS/LP measurements. *Atmospheric Measurement Techniques*, 9, 1239–1246.
825 <https://doi.org/10.5194/amt-9-1239-2016>
- 826 Degenstein, D. A., Bourassa, A. E., Roth, C. Z., & and Llewellyn, E. J. (2009).: Limb scatter ozone
827 retrieval from 10 to 60 km using a multiplicative algebraic reconstruction technique., *Atmospheric*
828 *Chemistry and Physics*, 9, 6521–6529, <https://doi.org/10.5194/acp-9-6521-2009>, 2009.
- 829 DeLand, M. T., & Gorkavyi, N. (2020). PMC observations from the OMPS Limb Profiler. *Journal*
830 *of Atmospheric and Solar-Terrestrial Physics*, 213, 105505.
831 <https://doi.org/10.1016/j.jastp.2020.105505>
- 832 Farman, J. C., Gardiner, B. G., & Shanklin, J. D. (1985). Large losses of ozone in Antarctica reveal
833 seasonal ClO_x/NO_x interaction. *Nature*, 315, 207–210. <https://doi.org/10.1038/315207a0>
- 834 Fisher, B. L., Lamsal, L. N., Fasnacht, Z., Oman, L. D., Joiner, J., Krotkov, N. A., et al. (2024).
835 Revised estimates of NO₂ reductions during the COVID-19 lockdowns using updated TROPOMI
836 NO₂ retrievals and model simulations. *Atmospheric Environment*, 326, 120459,
837 <https://doi.org/10.1016/j.atmosenv.2024.120459>.
- 838 Flittner, D. E., Bhartia, P. K., & Herman, B. M. (2000). O₃ profiles retrieved from limb scatter
839 measurements: Theory. *Geophysical Research Letters*, 27, 2601–2604.
840 <https://doi.org/10.1029/1999GL011343>
- 841 Flynn, L. E., Seftor, C. J., Larsen, J. C., & Xu, P. (2006). The ozone mapping and profiler suite.
842 In J. J. Qu, W. Gao, M. Kafatos, R. E. Murphy, & V. V. Salomonson (Eds.), *earth science satellite*
843 *remote sensing* (pp. 279–296). Berlin, Heidelberg: Springer. [https://doi.org/10.1007/978-3-540-](https://doi.org/10.1007/978-3-540-37293-6_15)
844 [37293-6_15](https://doi.org/10.1007/978-3-540-37293-6_15)
- 845 Gorshelev, V., Serdyuchenko, A., Weber, M., Chehade, W., & Burrows, J. P. (2014). High spectral
846 resolution ozone absorption cross-sections – Part 1: Measurements, data analysis and comparison
847 with previous measurements around 293 K. *Atmospheric Measurement Techniques*, 7, 609–624.
848 <https://doi.org/10.5194/amt-7-609-2014>
- 849 Herman, B. M., Ben-David, A., & Thome, K. J. (1994). Numerical techniques for solving the
850 radiative transfer equation for a spherical shell atmosphere. *Applied Optics*, 33, 1760–1770.
851 <https://doi.org/10.1364/AO.33.001760>
- 852 Janz, S. J., Hilsenrath, E., Flittner, D. E., & Heath, D. F. (1996). Rayleigh scattering attitude sensor,
853 Proceedings of SPIE 2831, Atmospheric Ultraviolet and Space Remote Sensing: Methods and
854 Instrumentation, 146. <https://doi.org/10.1117/12.257207>

- 855 Jaross, G., Bhartia, P. K., Chen, G., Kowitt, M., Haken, M., Chen, Z., et al. (2014). OMPS Limb
856 Profiler instrument performance assessment. *Journal of Geophysical Research: Atmospheres*, 119,
857 4399–4412. <https://doi.org/10.1002/2013JD020482>
- 858 Kramarova, N. A., & DeLand, M. (2023). README Document for the Suomi-NPP OMPS LP L2
859 O3 Daily Product (Version 2.6). Goddard Earth Sciences Data and Information Services Center
860 (GES DISC) (36 pp.). Retrieved from
861 [https://disc.gsfc.nasa.gov/datasets/OMPS_NPP_LP_L2_O3_DAILY_2.6/summary?keywords=O](https://disc.gsfc.nasa.gov/datasets/OMPS_NPP_LP_L2_O3_DAILY_2.6/summary?keywords=OMPS)
862 [MPS](https://disc.gsfc.nasa.gov/datasets/OMPS_NPP_LP_L2_O3_DAILY_2.6/summary?keywords=OMPS)
- 863 Kramarova, N. A., Bhartia, P. K., Jaross, G., Moy, L., Xu, P., Chen, Z., et al. (2018). Validation
864 of ozone profile retrievals derived from the OMPS LP version 2.5 algorithm against correlative
865 satellite measurements, *Atmospheric Measurement Techniques*, 11, 2837–2861.
866 <https://doi.org/10.5194/amt-11-2837-2018>
- 867 Kramarova, N. A., Nash, E. R., Newman, P. A., Bhartia, P. K., McPeters, R. D., Rault, D. F., et
868 al. (2014). Measuring the Antarctic ozone hole with the new Ozone Mapping and Profiler Suite
869 (OMPS). *Atmospheric Chemistry and Physics*, 14, 2353–2361. [https://doi.org/10.5194/acp-14-](https://doi.org/10.5194/acp-14-2353-2014)
870 [2353-2014](https://doi.org/10.5194/acp-14-2353-2014)
- 871 Livesey, N. J., Read, W. G., Wagner, P. A., Froidevaux, L., Santee, M. L., Schwartz, M. J., et al.
872 (2022). Version 5.0x Level 2 and 3 data quality and description document (Tech. Rep. No. JPL D-
873 105336 Rev. B). Jet Propulsion Laboratory. Retrieved from [https://mls.jpl.nasa.gov/data/v5-](https://mls.jpl.nasa.gov/data/v5-0_data_quality_document.pdf)
874 [0_data_quality_document.pdf](https://mls.jpl.nasa.gov/data/v5-0_data_quality_document.pdf)
- 875 Livesey, N. J., Snyder, W. V., Read, W. G., & Wagner, P. A. (2006). Retrieval algorithms for the
876 EOS Microwave Limb Sounder (MLS). *IEEE Transactions on Geoscience and Remote Sensing*,
877 44 (5), 1144–1155. <https://doi.org/10.1109/TGRS.2006.872327>
- 878 Loughman, R. P., Flittner, D. E., Herman, B. M., Bhartia, P. K., Hilsenrath, E., & McPeters, R. D.
879 (2005). Description and sensitivity analysis of a limb scattering ozone retrieval algorithm. *Journal*
880 *of Geophysical Research: Atmospheres*, 110, D19301. <https://doi.org/10.1029/2004JD005429>
- 881 Loughman, R., Bhartia, P. K., Chen, Z., Xu, P., Nyaku, E., & Taha, G. (2018). The Ozone Mapping
882 and Profiler Suite (OMPS) Limb Profiler (LP) Version 1 aerosol extinction retrieval algorithm:
883 theoretical basis. *Atmospheric Measurement Techniques*, 11, 2633–2651,
884 <https://doi.org/10.5194/amt-11-2633-2018>
- 885 Loughman, R., Flittner, D., Nyaku, E., & Bhartia, P.K. (2015). Gauss-Seidel Limb Scattering
886 (GSLs) radiative transfer model development in support of the Ozone Mapping and Profiler Suite
887 (OMPS) Limb Profiler mission. *Atmospheric Chemistry and Physics*, 15, 3007–3020,
888 <https://doi.org/10.5194/acp-15-3007-2015>
- 889 Lucchesi, R. (2013). File Specification for GEOS-5 FP-IT. GMAO Office Note No. 2 (Version
890 1.2) (60 pp.). Retrieved from http://gmao.gsfc.nasa.gov/pubs/office_notes
- 891 McPeters, R. D., & Labow, G. J. (2012). Climatology 2011: An MLS and sonde derived ozone
892 climatology for satellite retrieval algorithms. *Journal of Geophysical Research: Atmospheres*,
893 117(10), D10303, <https://doi.org/10.1029/2011JD017006>

- 894 McPeters, R. D., Janz, S. J., Hilsenrath, E., & Brown, T. L. (2000). The retrieval of O₃ profiles
895 from limb scatter measurements: Results from the Shuttle Ozone Limb Sounding Experiment.
896 *Geophysical Research Letters*, 27(17), 2597–2600. <https://doi.org/10.1029/1999GL011342>
- 897 Mérienne, M. F., Jenouvier, A., & Coquart, B., (1995). The NO₂ absorption spectrum. I:
898 Absorption cross-sections at ambient temperature in the 300-500 nm region. *Journal of*
899 *Atmospheric Chemistry*, 20, 281–297. <https://doi.org/10.1007/BF00694498>
- 900 Millán, L., Santee, M. L., Lambert, A., Livesey, N. J., Werner, F., Schwartz, M. J., et al. (2022).
901 The Hunga Tonga-Hunga Ha'apai Hydration of the Stratosphere. *Geophysical Research Letters*,
902 49, e2022GL099381. <https://doi.org/10.1029/2022GL099381>
- 903 Moy, L., Bhartia, P. K., Jaross, G., Loughman, R., Kramarova, N., Chen, Z., et al. (2017). Altitude
904 registration of limb-scattered radiation. *Atmospheric Measurement Techniques*, 10, 167–178.
905 <https://doi.org/10.5194/amt-10-167-2017>
- 906 NASA. (2023). NASA's Terra, Aqua, and Aura Data Continuity Workshop, Workshop Summary.
907 Retrieved from <https://nspires.nasaprs.com/external/viewrepositorydocument/cmdocumentid=985170/solicitationId=%7BEC26B6F5-5B02-8932-45F4-EAF5DED2DA14%7D/viewSolicitationDocument=1/Terra-Aqua-Aura-Data-Continuity-RFI-and-Workshop-Summary2.pdf>
- 908
909
910
911
- 912 Nielsen, J. E., Pawson, S., Molod, A., Auer, B., da Silva, A. M., Douglass, A. R., et al. (2017).
913 Chemical mechanisms and their applications in the Goddard Earth Observing System (GEOS)
914 earth system model. *Journal of Advances in Modeling Earth Systems*, 9(8), 3019–3044.
915 <https://doi.org/10.1002/2017MS001011>
- 916 Orbe, C., Oman, L. D., Strahan, S. E., Waugh, D. W., Pawson, S., Takacs, L. L., & Molod, A. M.
917 (2017). Large-scale atmospheric transport in GEOS replay simulations. *Journal of Advances in*
918 *Modeling Earth Systems*, 9, 2545–2560. <https://doi.org/10.1002/2017MS001053>
- 919 Prather, M., & Jaffe, A. H. (1990). Global impact of the Antarctic ozone hole: Chemical
920 propagation. *Journal of Geophysical Research: Atmospheres*, 95, 3473–3492.
921 <https://doi.org/10.1029/JD095iD04p03473>
- 922 Rault, D. F. (2005). Ozone profile retrieval from Stratospheric Aerosol and Gas Experiment
923 (SAGE III) limb scattering measurements. *Journal of Geophysical Research: Atmospheres*, 110,
924 D09309. <https://doi.org/10.1029/2004JD004970>
- 925 Rault, D. F., & Loughman, R. P. (2013). The OMPS Limb Profiler Environmental Data Record
926 Algorithm Theoretical Basis Document and Expected Performance. *IEEE Transactions on*
927 *Geoscience and Remote Sensing*, 51(5), 2505-2527. <https://doi.org/10.1109/TGRS.2012.2213093>
- 928 Rodgers, C. D. (2000). *Inverse methods for atmospheric sounding: Theory and practice* (p. 238).
929 World Scientific.

- 930 Schoeberl, M. R., Wang, Y., Ueyama, R., Taha, G., & Yu, W. (2023). The cross equatorial
931 transport of the Hunga Tonga-Hunga Ha'apai eruption plume. *Geophysical Research Letters*,
932 50(4), e2022GL102443. <https://doi.org/10.1029/2022GL102443>
- 933 Stolarski, R. S., Krueger, A. J., Schoeberl, M. R., McPeters, R. D., Newman, P. A., & Alpert, J.
934 C. (1986). Nimbus 7 satellite measurements of the springtime Antarctic ozone decrease. *Nature*,
935 322, 808–811. <https://doi.org/10.1038/322808a0>
- 936 Taha, G., Jaross, G., Fussen, D., Vanhellemont, F., Kyrölä, E., & McPeters, R. D. (2008). Ozone
937 profile retrieval from GOMOS limb scattering measurements. *Journal of Geophysical Research:*
938 *Atmospheres*, 113, D23307. <https://doi.org/10.1029/2007JD009409>
- 939 Taha, G., Loughman, R., Colarco, P. R., Zhu, T., Thomason, L. W., & Jaross, G. (2022). Tracking
940 the 2022 Hunga Tonga-Hunga Ha'apai aerosol cloud in the upper and middle stratosphere using
941 space-based observations. *Geophysical Research Letters*, 49, e2022GL100091.
942 <https://doi.org/10.1029/2022GL100091>
- 943 Vandaele, A. C., Hermans, C., Simon, P. C., Carleer, M., Colin, R., Fally, S., et al. (1998).
944 Measurements of the NO₂ absorption cross-section from 42 000 cm⁻¹ to 10 000 cm⁻¹ (238–1000
945 nm) at 220 K and 294 K. *Journal of Quantitative Spectroscopy and Radiative Transfer*, 59, 171–
946 184. [https://doi.org/10.1016/S0022-4073\(97\)00168-4](https://doi.org/10.1016/S0022-4073(97)00168-4)
- 947 Wargan, K., Kramarova, N., Weir, B., Pawson, S., & Davis, S. M. (2020). Toward a reanalysis of
948 stratospheric ozone for trend studies: Assimilation of the Aura microwave limb sounder and ozone
949 mapping and profiler suite limb profiler data. *Journal of Geophysical Research: Atmospheres*,
950 125(4), e2019JD031892. <https://doi.org/10.1029/2019JD031892>
- 951 WMO (World Meteorological Organization). (2022). *Scientific Assessment of Ozone Depletion:*
952 *2022* (GAW Report No. 278, 509 pp.). Geneva: WMO. Retrieved from
953 <https://ozone.unep.org/science/assessment/sap>
- 954 Xu, P. Q., Bhartia, P. K., Jaross, G. J., DeLand, M. T., Larsen, J. C., Fleig, A., et al. (2014). Release
955 2 data products from the Ozone Mapping and Profiling Suite (OMPS) Limb Profiler. Proceedings
956 of SPIE 9242, Remote Sensing of Clouds and the Atmosphere XIX; and Optics in Atmospheric
957 Propagation and Adaptive Systems XVII, 92420K. <https://doi.org/10.1117/12.2067320>
- 958 Ziemke, J. R., Labow, G. J., Kramarova, N. A., McPeters, R. D., Bhartia, P. K., Oman, L. D., et
959 al. (2021). A global ozone profile climatology for satellite retrieval algorithms based on Aura MLS
960 measurements and the MERRA-2 GMI simulation. *Atmospheric Measurement Techniques*, 14,
961 6407–6418. <https://doi.org/10.5194/amt-14-6407-2021>
962